

SENTINEL-3 OPTICAL PRODUCTS AND ALGORITHM DEFINITION

ACTIVE FIRE: FIRE DETECTION AND FIRE RADIATIVE POWER ASSESSMENT

DOCUMENT REF: S3-L2-SD-03-T04-KCL-ATBD_FIREPRODUCT

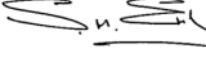
DELIVERABLE REF: SD-03-T

VERSION: 3.2

CREATION DATE: 2009-07-09

LAST MODIFIED: 2012-10-10

DOCUMENT SIGNATURE TABLE

	NAME	FUNCTION	INSTITUTION	SIGNATURE AND DATE
PREPARED	M.J. Wooster W. Xu	Consultant	King's College London	 10-10-2012
VERIFIED	S. Emsley	Project Manager	ARGANS	 10-10-2012
APPROVED				

DOCUMENT DIFFUSION LIST

ORGANISATION	NAME
ESA	Philippe Goryl, Alessandra Buongiorno and Carla Santella
EUMETSAT	Vincent Fournier-Sicre and Vincenzo Santacesaria
Consortium Partners	ARGANS, ACRI-ST, RAL, Brockmann-Consult, Elsag-Datamat

DOCUMENT CHANGE RECORD

VERSION	DATE	AUTHOR	DESCRIPTION
1.0	20/07/2009	M.J. Wooster & W. Xu	PDR (initial version)
3.1	10/06/2010	M.J. Wooster & W. Xu	CDR update
3.2	10/10/2012	M.J. Wooster & W. Xu	FR Update

Table of Contents

1.1. INTRODUCTION	6
1.1 Acronyms and Abbreviations	7
1.2 Purpose and Scope	9
1.3 Algorithm Identification	12
1.4 Algorithm Heritage	15
2. ALGORITHM OVERVIEW – PHYSICS OF THE PROBLEM	15
2.1 Background	17
2.1.1 Fire Detection Principles.....	18
2.1.2 Fire Characterisation Principles	20
3. ALGORITHM DESCRIPTION.....	24
3.1 Overview of Algorithm Structure	24
3.2 Detection of Potential Fire Pixels (Stage 1)	27
3.2.1 Spectral Filter Detail (Stage 1a)	28
3.2.2 Spatial Filter Detail (Stage 1b)	30
3.3 Background Characterisation (Stage 2)	32
3.4 Fire Pixel Confirmation (Stage 3)	34
3.4.1 Absolute Threshold Test (Stage 3a)	34
3.4.2 Contextual Threshold Tests (Stage 3b)	37
3.5 False Alarm Elimination (Stage 4)	39
3.5.1 Sun Glint Identification (Stage 4a)	39
3.5.2 Desert Boundary Rejection (Stage 4b)	40
3.6 Fire Characterisation (Stage 5)	41

4	UNCERTAINTY BUDGET	41
4.1	FRP Error Estimation and Fire Pixel Confidence Assessment (Stage 6)	41
4.1.1	FRP Error Estimation.....	41
4.1.2	Fire Pixel Confidence Assessment.....	42
5.	PRACTICAL CONSIDERATIONS.....	45
5.1	Cloud Masking.....	45
5.2	Water Masking.....	46
6.	EVOLUTION	47
7.	ASSUMPTIONS AND LIMITATIONS	53
8.	INPUTS AND OUTPUTS	54
9.	VALIDATION.....	55
10.	REFERENCES	57
8.	APPENDIX A: SENTINEL-3 SLSTR CHANNEL NAMING CONVENTION.....	62

List of Figures

1. Fire location and timing recorded across Africa by Meteosat SEVIRI.
2. Diurnal cycle of total fire radiative power recorded across Africa by Meteosat SEVIRI.
3. Spectral radiance emitted from blackbodies.
4. MIR (3.7 μm) and TIR (10.8 μm) brightness temperatures for modelled fire pixels
5. Spectral radiance at a MIR wavelength (3.7 μm), and power law approximation.
6. Structure of the SLST Fire detection and characterisation algorithm
7. Example high pass spatial filter of 3 x 3 pixel size.
8. Example result of fire detection
9. Example result of gas flare detection
10. Example result of gas flare detection

1 INTRODUCTION

This document describes the theory for the prototype multi-channel active fire detection and fire characterisation algorithm for use with data from the SLSTR sensor onboard the ESA Sentinel-3 satellite. It therefore provides a detailed description of the algorithm to be used in the production of the SLSTR Active Fire Product, which consists of both Active Fire Detection and Fire Radiative Power assessment. The algorithm was initially designed to detect and characterise vegetation fires burning on the land surface land, though it will also very likely identify some sites of active volcanism and high temperature industrial heat sources due to the similarity of their multi-spectral signatures to those of vegetation combustion. In response to user requests, the version of the algorithm described here was updated to take into account the potential for the detection of offshore gas flares (i.e. detection of hotspots over the open ocean and in coastal regions and potentially large lakes). The characterisation of vegetation fires is undertaken via a calculation of their fire radiative power (FRP) output, a measure of their total radiative power output integrated over all wavelengths and angles. FRP is also calculated for other detected hotspots, though its scientific use has not been confirmed for non-vegetation fire targets. For simplicity, the different classes of hotspot potentially detectable by the algorithm are here referred to simply as “Land Hotspots” and “Ocean hotspots”, and in the detailed description of the tests the word “fire” is generally used to refer to all types of hotspot potentially encountered.

The burning of vegetation, together with surface organic matter such as carbon-rich peatland soils, occurs annually across many millions of square kilometres of the Earth surface and perturbs a greater area over a wider variety of biomes than any other natural disturbance agent (Lavorel *et al.*, 2006). The widespread nature, and sporadic, unpredictable character of fire, means that frequent data from Earth Observation (EO) satellites are key to providing the data necessary for the large-scale investigation and quantification of biomass burning and its effects, such as the resulting emissions to the atmosphere of carbon, trace gases and aerosol. The SLSTR Active Fire algorithm is designed to produce two of the measurements highlighted by the UNFCCC-defined Essential Climate Variables related to ‘Fire Disturbance’, namely *Active Fire* [detection] and *Fire Radiative Power* [fire characterisation] (Sessa and

Dolman, 2008; Csizar *et al.*, 2008). *Active Fire* records the time and location of fires that were burning as the sensor imaged the land surface, expressed either in spatial and temporal coordinates or by an indicator of fire presence or absence in a raster map. Active fire detections are used, for example, to identify fire emissions source locations and timings, to determine fire-related parameters within ecosystem models having a representation of fire (such as fire rate of spread), and to identify fire seasonal cycles and spatio-temporal trends, potentially in relation to environmental variations such as climate change (e.g. Levine *et al.*, 1996a, 1996b; Kaufman *et al.*, 1998; Wooster and Strub, 2002; Sukhinin *et al.*, 2004; Csizar *et al.*, 2005; Giglio *et al.*, 2006a, Giglio *et al.*, 2006b; Lodoba and Csizar, 2007). Fire Radiative Power (FRP) is the rate at which the actively burning fire is emitting radiative energy [at the time of observation] expressed in units of power (Js^{-1} or Watts). Through a series of airborne, ground-based and satellite data intercomparisons, FRP has been shown to be well related to the rate of fuel consumption, smoke aerosol production, and trace gas release, and thus offers a direct route to quantifying the magnitude of these processes (Kaufman *et al.*, 1998; Wooster *et al.*, 2005; Ichoku and Kaufman, 2005; Jordan *et al.*, 2007; Freeborn *et al.*, 2008).

1.1 Acronyms and Abbreviations

AVHRR Advanced Very High Resolution Radiometer

ATBD Algorithm Theoretical Basis Document

(A)ATST (Advanced) Along track Scanning Radiometer

BT Brightness Temperature

CLM CLoud Mask

EO Earth Observation

ECV Essential Climate Variable

FRP Fire Radiative Power

FRE Fire Radiative Energy

GTOS Global Terrestrial Observing System

LUT Look-Up Table

LWIR Longwave InfraRed

MAD Mean Absolute Deviation

MIR Middle InfraRed

MODIS Moderate-Resolution Imaging Spectroradiometer

PSF Point Spread Function

ROI Region of Interest

SLSTR Sea and Land Surface Temperature Radiometer

TIR Thermal InfraRed

VIS Visible spectral region

The Sentinel-3 SLSTR channel naming convention and matching scientific notation used throughout this document is detailed in Appendix A.

1.2 Purpose and Scope

Open vegetation fires are critical elements in the Earth System, acting as a widespread agent of change by altering land cover properties and consuming very significant quantities of terrestrial vegetation and releasing copious amounts of trace gases and aerosols (Lavorel *et al.*, 1996). Such fire activity acts across all vegetated continents but is often highly variable in its magnitude and specific location, making satellite EO data key in its quantification (Bond and van Wilgen, 1996). A marked seasonality is also often present in response to seasonal climate variations, as Figure 1 demonstrates. Data on fire activity is used within many areas of terrestrial environmental research, such as for prescribing the source terms for regional or global atmospheric emissions of carbon, trace gases and aerosols, and for developing periodic assessments of land cover changes such as tropical deforestation. The information is also used in fire and ecosystem management planning and operation (such as fire use, preparedness and wildfire suppression) and for informed policy development (Csiszar *et al.*, 2008).

Polar-orbiting imaging sensors such as the Sentinel-3 SLSTR can provide data on each of the ‘Fire Disturbance’ Essential Climate Variables (ECVs) identified by the Global Terrestrial Observing System (GTOS) as being necessary for determining transient change, adaptation, impact and mitigation possibilities in relation to climate and associated environmental changes, namely *Burned Area*, *Active Fire* and *Fire Radiative Power* (Sessa and Dolman, 2008). This ATBD describes the prototype algorithm for use in deriving the *Active Fire* and *Fire Radiative Power* variables. The SLSTR spectral bands in the solar reflected and thermal emissive parts of the electromagnetic spectrum allow it to deliver these ECVs using a consistent, standardised set of algorithms operating over the entire Earth, frequently and repetitively.

Individual pixels containing active fires are detected based on the identification thermal channel signals characteristic of active fires, with signals in the sensors solar reflective channels used to decrease the probability of false alarms from features such as sunglint from small water bodies. Estimates of the FRP being emitted by the detected fire pixel are made via assessment of the thermal channel signal increase over surrounding the non-fire

background pixels, using the MIR radiance approach developed by Wooster et al. (2003) and applied operationally in the SEVIRI FRP product (Roberts and Wooster, 2008).

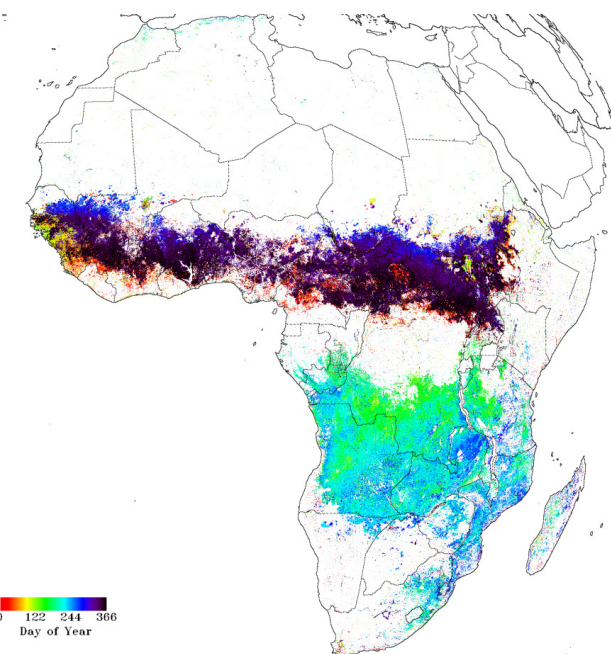


Figure 1. Fire location and timing across Africa as derived from the operational Meteosat SEVIRI Fire Radiative Power product delivered by the Land Satellite Applications Facility (Roberts and Wooster, 2008; <http://landsaf.meteo.pt/>). The marked seasonality follows the dry seasons in north and southern Africa.

Geostationary EO satellites provide the highest temporal resolution active fire data, and the EUMETSAT Land Surface Analysis Satellite Applications Facility (<http://landsaf.meteo.pt/>) provides near real-time active fire and FRP data for Africa, Europe and parts of South America from the Meteosat Second Generation series of geostationary satellites (Figure 1). These data can be used to demonstrate the marked fire diurnal cycle seen in many environments (Figure 2), and indicate the necessity to detect fires by daytime when they are most active – not just during the night time when detection is typically somewhat easier due to the cooler background and lack of incoming solar radiation. However, despite their many attractions, geostationary systems are limited in their ability to detect and characterise the smaller and/or less intensely burning component of the active fire regime, due to their coarse spatial resolution, yet these types of fire are more common than are the largest, highest

intensity events. Since assessment of the full extent of fire activity is central to providing accurate and reliable data for environmental science and policy development, active fire observations from higher spatial resolution polar orbiting sensors such as SLSTR remain essential. Furthermore, not all current geostationary sensors possess the IR channel sensor characteristics necessary to detect and characterise active fires, so large gaps remain in the global record, and the view from geostationary orbit offers poor coverage of key fire-affected areas at higher latitudes (i.e. the boreal zone). The SLSTR Fire Product will therefore provide important data to support the generation of a long-term, global-scale ‘Fire Disturbance’ EVC record that will allow characterisation of the fullest extent of Earth’s fire regime. In response to user requests, the version of the algorithm described here is also designed with the potential to detect offshore gas flares (i.e. detection of hotspots over the open ocean and in coastal regions) due to potential interest in monitoring the extent of such industrial combustion activity.

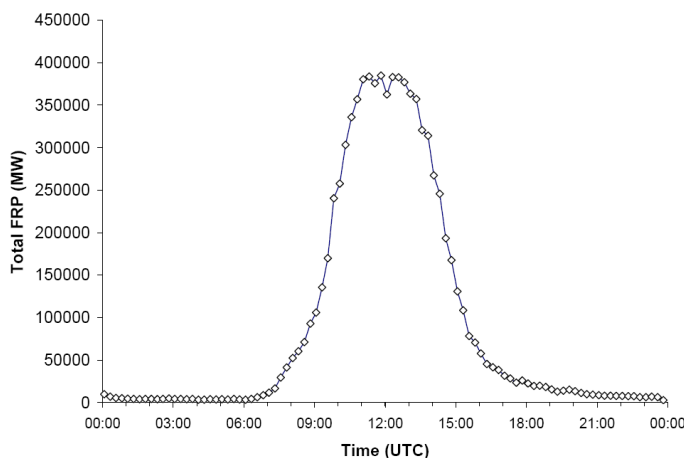


Figure 2. Diurnal cycle of total fire radiative power recorded by the Meteosat SEVIRI FRP product across southern Africa every 15 minutes on 14 July 2004. Local time across the region is up to three hours in advance of UTC. A very strong fire diurnal cycle is clearly evident. At the peak, the fires detected across the region were located in around 5000 fire pixels and were producing a combined FRP of 382 GW. When adjusted for the effects of cloud cover, atmospheric absorption and the presence of undetected smaller/low intensity fires this suggests that at least 250 tonnes of vegetation per second was being burned in order to generate this radiant energy release (Wooster *et al.*, 2005).

1.3 Algorithm Identification

When observed from space with moderate spatial resolution instruments (~ kilometre scale pixels such as those of SLSTR), actively burning fires represent sub-pixel features; typically covering only a very small fraction of the individual detector ground field of view. Optimum active fire detection in such circumstances generally requires that the sensor possesses spectral channels in the middle-infrared (MIR; 3-5 μm) and thermal-infrared (TIR; 8-12 μm). Data from solar reflective (VIS) channels are used to assist with false alarm identification, for example by removing pixels affected by sunglint whose strong MIR signals can look very similar to those of fire pixels. Potential fire pixels can be identified via multi-channel thresholding of the TIR, MIR and VIS band data, but if the algorithm is to remain effective over large areas, as well as through seasonal cycles, the specific thresholds used must be allowed to vary with environmental condition (Flasse and Ceccato, 1996). For this reason, a self-adaptive, contextual fire detection scheme whose thresholds vary in response to the background signals recorded at confirmed non-fire pixels has been identified as the most effective approach for use with SLSTR.

Once detected, the FRP can be estimated from the fire pixel signal increases measured in the sensors thermal channel(s). Generally this is assessed with respect to the neighbouring ambient background signal. One candidate for a method to estimate the FRP is simply the Stefan-Boltzmann Law, but this requires the instantaneous fire effective temperature (T_f) and sub-pixel fractional area (p_f) [since the fires are not resolved at the scale of SLSTR pixels]. These parameters can be determined using the so-called bi-spectral approach, based on simultaneous TIR and MIR channel radiance measurements made at the fire pixel and at the surrounding non-fire pixels, and this method has been used to retrieve FRP from data collected by the Bi-Spectral Infrared Detection (BIRD) Hot-Spot Recognition System (HSRS) Satellite, as well as from various other spaceborne and airborne sensors (Zhukov *et al.*, 2006). However, fire signals in the TIR channel are much weaker than in the MIR channel, yet the bi-spectral approach requires that both be well characterised for optimum retrieval accuracy. As a result, bi-spectral retrievals can be subject to large errors when variability in the TIR brightness temperatures of the non-fire background pixels means that the degree to which the fire pixel TIR channel signal is raised above the TIR background signal cannot be precisely determined (Giglio and Kendall, 2001; Wooster *et al.*, 2003). This

effect will typically be much more significant for the kilometre scale SLSTR pixels than for the BIRD HSRS pixels that were 10x smaller in area, since a particular fire will represent a smaller proportional area in a larger pixel and will thus increase the fire pixel signal by a lesser amount. In addition, Shephard and Kennelly (2003) indicate the significant impact that band-to-band co-registration errors have on fire characterisation retrievals made with the bi-spectral method. They demonstrate that for a 1-km horizontal spatial resolution pixel, a 10% inter-channel co-registration error generates retrieval errors of the order of 150 K and 210 % for the effective fire temperature and fractional fire area terms respectively. In the BIRD HSRS processing chain, this effect was dealt with by clustering spatially contiguous fire pixels, and analysing the mean MIR and TIR signals recorded at the cluster scale to estimate the instantaneous cluster effective temperature (T_f) and sub-pixel area (A_f), rather than deriving per-pixel measures (Zhukov *et al.*, 2006). In this way the sensitivity to band-to-band co-registration errors was reduced considerably. However, because of the constraints of the bi-spectral approach, especially when applied to coarser scale remote sensing data, the MODIS fire products used a non-linear, empirical relationship between FRP and the fire pixel MIR brightness temperature increase above the background to derive FRP (Kaufman *et al.*, 1998). This relationship was itself derived using multiple simulations of MODIS observations of sub-pixel sized fires (Kaufman *et al.*, 1998). By using only a single waveband, the effect of inter-channel co-registration errors is removed, and by using the MIR waveband where the fire signal is strongest the errors induced due to uncertainty in the ambient background signal are minimised.

A new algorithm for FRP estimation was derived by Wooster *et al.* (2003), by approximating the Planck Function at MIR wavelengths by a power law valid over the range of temperatures seen in open vegetation fires. In this so-called ‘MIR radiance method’, FRP is linearly related to the fire pixel MIR radiance increase above the surrounding non-fire background. Wooster *et al.* (2003) used BIRD data to show that the MIR radiance method produced FRP estimates that agreed well with those from the bi-spectral method, as long as fire temperatures exceed ~ 650 K, which is generally the case for all but the most weakly smouldering events. Wooster *et al.* (2003) also demonstrated the approach to be capable of producing reliable FRP retrievals in cases where the bi-spectral approach was severely affected by large variability in the brightness temperatures of the ambient background. The

MIR radiance method has been adopted for use with the Meteosat FRP Pixel product produced operationally at the EUMTESAT LandSAF (Roberts and Wooster, 2008) and will be the approach used here for characterisation of active fire data from SLSTR.

1.4 Algorithm Heritage

Though it was designed with the key purpose of providing long-term, highly accurate observations of sea surface temperature (SST), the (A)ATSR series of sensors that are the heritage instruments for SLSTR do possess the MIR and TIR spectral channels necessary for fire detection, though their relatively low dynamic range (optimised for cloud and SST measurements) meant that daytime saturation of the MIR channel over warm terrestrial surfaces restricted routine active fire detection to night time only. Nevertheless, the resulting ATSR World Fire Atlas (WFA) is currently the longest available global active fire dataset (Orino *et al.*, 2007) and have been used to support databases representing the global fire emissions record (e.g. Van der Werf *et al.*, 2006) as well as a wide range of science studies (e.g. Thompson *et al.*, 2001; Schultz, 2002; Generoso *et al.*, 2003; Sinha *et al.*, 2004). However, the simple fixed threshold approach used within the WFA is far from optimum when considering the algorithmic possibilities for use with the SLSTR fire product, which is required to operate under a wide range of environmental conditions by day as well as by night. Daytime thermal conditions vary much more markedly between areas and over time than do night time conditions, and a contextual approach with self-adapting detection thresholds is required for optimum fire detection performance and false alarm minimisation. The MODIS fire detection algorithm (Giglio *et al.*, 2003) works on these principles, as does the BIRD HSRS fire detection scheme (Zhukov *et al.*, 2006) and the geostationary fire detection algorithm of Roberts and Wooster (2008). The SLSTR fire detection algorithm is therefore based on this contextual, self-adapting approach, using and blending many of the tests originally formulated in these previous schemes but with adjustments for the specific spectral coverage provided by SLSTR and with new additions to take into account the detection of offshore gas flares in addition to land-based hotspots. Perhaps the most significant adjustment with respect to fire is the absence of a 3.9 μm channel on SLSTR, which necessitates the use of the shorter wavelength 3.7 μm MIR spectral band (S7 and F1) instead, and the fact that measurements from the 500 m spatial resolution SWIR bands (S5 and S6) are available to aid land hotspot detection at night (and ocean hotspot detection by

day). The well-tested MODIS fire detection algorithm of Giglio *et al.* (2003) is the basis for the majority of the detection tests applied here, since in terms of data for deriving active fire products MODIS is the currently operating sensor that most closely matches SLSTR. However, in order to attempt to maximise performance, the method for detection of a potential fire pixels has been adjusted to become less conservative than that used in the MODIS algorithm, whilst the spatial filter from the geostationary algorithm of Roberts and Wooster (2008) is used to constrain the number of potential fire pixels passed to the next algorithm stage. The coefficients of this spatial filter are taken from image blocks rather than the entire image, in a manner akin to the first stage of the BIRD HSRS algorithm (Zhukov *et al.*, 2006). Following fire detection, fires are characterized based on their FRP using the MIR radiance method of Wooster *et al.* (2003). Certain of the additions related to gas flare detection was informed by the work of Gallegos *et al.* (2007).

2 ALGORITHM OVERVIEW – THE PHYSICS

2.1 Background

Vegetation fires exhibit a wide temperature range, generated by activity from smouldering to intense flaming combustion, but flame radiometric temperatures of $\sim 750 - 1200$ K appear dominant (Sullivan *et al.*, 2003). Wien's Displacement Law indicates that the peak of thermal emission from such fires occurs in or close to the shortwave Infrared (SWIR; 1.6 – 2.5 μm) or Middle Infrared (MIR; 3 – 5 μm) atmospheric windows, depending upon the combustion temperature. Fires are typically very much more active by day than by night (Figure 2), and the presence of relatively strong solar reflective signals in the SWIR region by day means that fire detection algorithms are generally mostly focused on using the MIR signal (Robinson, 1991). Parameterisation of the Planck function with the temperatures indicative of open vegetation fires indicates that in the MIR spectral region the spectral emission from an open vegetation fire can be up to four orders of magnitude greater than that from the ambient temperature background (Figure 3). Since the SLSTR has a MIR band centered on 3.7 μm this band is the most suitable as the basis for fire detection.

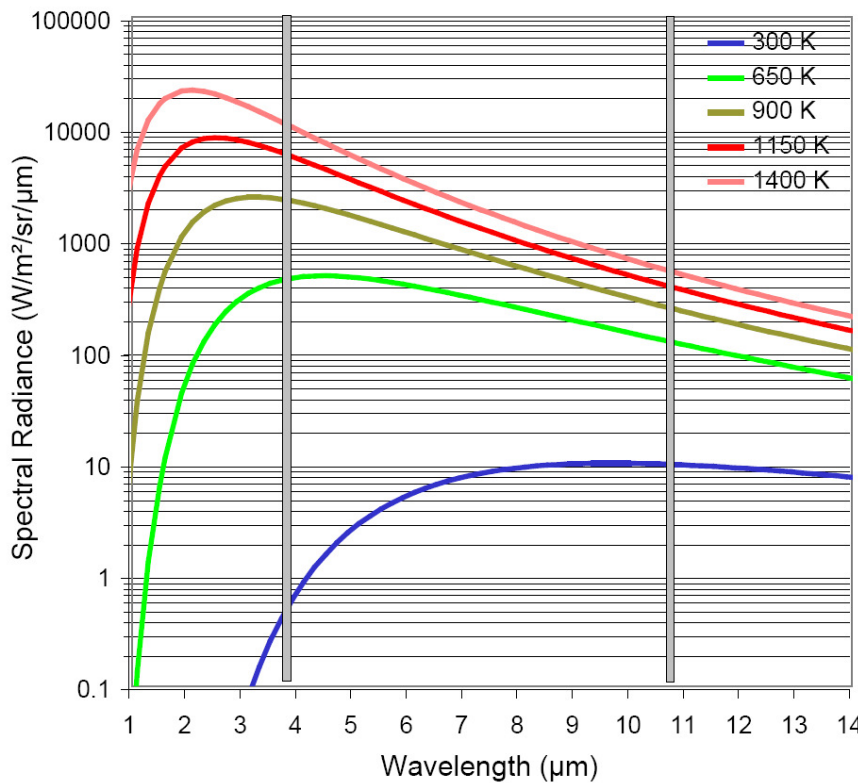


Figure 3. Spectral radiance emitted from blackbodies at Earth ambient temperature (300 K) and a range of possible vegetation fire temperatures (650 – 1400 K). The approximate central wavelengths of the SLSTR MIR (3.7 μm) and TIR1 (10.8 μm) channel are also indicated. As temperature increases the spectral radiance increases more rapidly at MIR wavelengths than at TIR wavelengths. Note the logarithmic y-axis scale.

The intense MIR thermal signals from combusting biomass means that pixels containing actively burning fires can be discriminated via their significant increase in MIR pixel radiance or brightness temperature, even if the fire covers only $10^{-3} - 10^{-4}$ of the pixel planimetric area (Robinson, 1991). This makes fire detection possible using even rather coarse spatial resolution data (e.g. from geostationary systems), or even from spatially-averaged Earth observation data such as AVHRR GAC imagery (e.g. Wooster and Strub, 2002). Fire pixels generally show elevated (Robinson, 2001). Fire detection algorithms are generally based on identification of an increased MIR channel signal and by their generally divergent MIR and TIR brightness temperatures, with other tests potentially added to optimize sensitivity.

FRP characterisation in addition requires that these channels used (especially the MIR channel) have a wide dynamic range such that they do not saturate. Under certain circumstances observations in the SLSTR SWIR bands (S5 and S6) can also be used to aid hotspot detection since as Figure 3 demonstrates objects at many hundreds of Kelvin above ambient temperatures emit significantly at these wavelengths, albeit by day over the land surface these emissions are usually eclipsed in magnitude by reflected solar radiation.

Care must be taken when designing hotspot detection algorithms however, since by day solar-heating on bare ground and specularly reflected sunlight can also increase MIR pixel signals far above those of surrounding areas, and thus especially by day active fire detection algorithms must use a series of additional multi-spectral optical and thermal channel tests to discriminate true fire pixels from such “false alarms”. Pixels that are homogeneously hot due to solar heating of, for example, bare rock or soil surfaces should have similar MIR and TIR brightness temperatures (albeit somewhat different due to differing atmospheric and surface emissivity and solar reflection effects). Pixels containing sub-pixel sized fires can have large MIR and TIR brightness temperature differences. Pixels that show a high MIR signal due to sunglint from (potentially sub-pixel sized) water bodies also show a markedly increased VIS channel signal, but pixels containing sub-pixel fires do not. Using such multispectral methods, true fire pixels can be discriminated from false alarms.

Such false alarm discrimination is required since using only nighttime data will markedly underestimate fire activity, and daytime fire detection is thus key (Figure 2). Once an active fire pixel is detected its radiative power can be determined from the signal increase induced by the fire compared to if the fire were not present. This requires unsaturated observations to be available in the sensors thermal channels, and thus generally necessitates a sensor with a wide dynamic range. The exact saturation temperature of the image will be inversely related to the size of the ground field of view. In the most extreme case, a very high spatial resolution sensor would allow the fire to be full resolved and thus the dynamic range would need to extend to ~ 1300 K. This is not the case for the moderate spatial resolution SLSTR sensor,

where the fires will very likely only cover a relatively small proportion of the pixel area.

2.1.1 *Fire Detection Principles*

Consider a pixels ground field of view of uniform background temperature T_b , containing a sub-pixel fire of effective radiant temperature T_f and effective fractional area P_f . Assuming a unitary emissivity and neglecting atmospheric and solar reflected radiation effects for the present case, the observed spectral radiance (L_λ) in two different spectral bands that can be approximated by central wavelengths in the MIR and TIR regions can be simply assumed to be the area weighted sum of that from the two individual thermal components (Dozier, 1981; Giglio and Justice, 2003).

$$L_{MIR} = p_f B(\lambda_{MIR}, T_f) + (1 - p_f) B(\lambda_{MIR}, T_b) \quad (1)$$

$$L_{TIR} = p_f B(\lambda_{TIR}, T_f) + (1 - p_f) B(\lambda_{TIR}, T_b) \quad (2)$$

Where $B(\lambda, T)$ is the Planck function at wavelength λ and temperature T .

Given the Planck function relationships shown in Figure 3, the presence of a subpixel sized fire within the ground FOV will enhance the pixel integrated spectral radiance (L_λ) much more in the MIR than in the TIR. Converting L_{MIR} and L_{TIR} into the equivalent brightness temperatures T_{MIR} and T_{TIR} through the inverse Planck function therefore results in $T_{MIR} \gg T_{TIR}$. The magnitude of this $T_{MIR} - T_{TIR}$ brightness temperature difference (which we here term $\Delta T_{MIR-TIR}$) increases with increasing T_f and p_f , up to the point where the fire starts to cover a very large proportion [>10%] of the pixel (Figure 4). A > 10% coverage by fire will be a very rare (potentially non-existent) occurrence for a moderate spatial resolution sensor such as SLSTR. Active fire detection algorithms are therefore generally based on thresholding pixel level observations of T_{MIR} and $\Delta T_{MIR-TIR}$ to discriminate fire pixels from non-fire pixels. Thresholds must be carefully chosen, since even certain non-fire pixels can have substantially increased values of T_{MIR} and $\Delta T_{MIR-TIR}$ due, for example, to intense solar

heating or where atmospheric and surface emissivity effects are large. An approach using fixed spatially and/or temporally thresholds is therefore not effective for an algorithm required to be applied globally across all regions and seasons and by day and by night, so a contextual approach is adopted whereby fire pixels are identified based on their signal contrast with the surrounding non-fire ambient ‘background’ pixels (Flasse and Ceccato, 1996). Strong contrast with the background in terms of the T_{MIR} and $\Delta T_{MIR-TIR}$ measures is the basic detection criteria, with additional multi-spectral tests using both TIR and VIS channels aimed at preventing false alarms from, for example, uniformly warm surfaces and reflected sun glint.

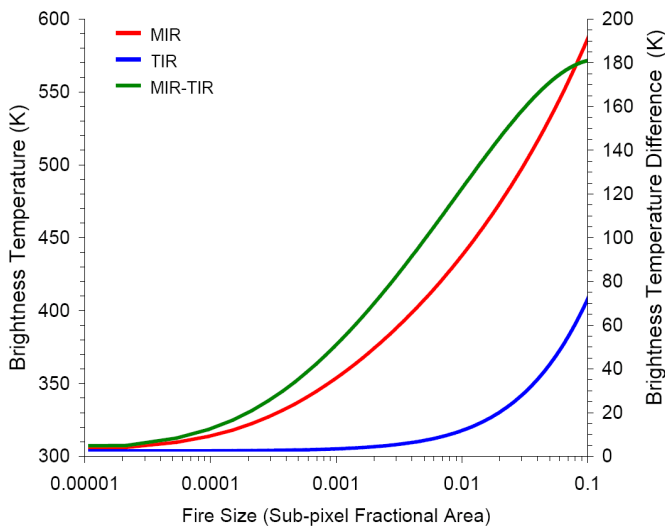


Figure 4: MIR (3.7 μm) and TIR (10.8 μm) brightness temperatures for a pixel containing an active fire of effective BT 900 K, superimposed on an ambient background of 300 K. As the proportional area of the pixel covered by the fire increases, the BT measured in both spectral channels also increases, but more rapidly in the MIR channel due to the fires spectral radiance signal peaking in this wavelength region. Thresholding of the MIR-TIR BT difference between these two spectral channels is commonly used to detect such active fire pixels. Fires of this temperature covering even 10^{-3} of a pixel are seen to raise the pixels MIR-TIR BT difference by more than 10 K. Emissivity and atmospheric effects have been neglected in this calculation.

2.1.2 Fire Characterisation Principles

Once an active fire pixel has been detected, it can be characterised through estimation of its fire radiative power. As previously described, FRP quantifies the rate of release of radiant energy by a fire over all wavelengths and angles. However, SLSTR measures the fire pixel signal in only a few discrete wavebands and in one viewing direction. Two approaches to address the estimation of FRP from such data are the bi-spectral method coupled to the Stefan-Boltzmann Law, which exploits the differential fire signal in two or more co-registered spectral channels (Dozier 1981), or single channel approaches that exploit the signal in the MIR channel only (Wooster et al., 2003). All approaches assume the fire energy emission is essentially lambertian. For the reasons stated earlier, at the present time the SLSTR algorithm will adopt the single channel MIR radiance method for fire characterisation originally presented in Wooster *et al.* (2003) due to its relatively moderate spatial resolution and the influence on the bi-spectral method of background ‘clutter’ in the TIR channel and its sensitivity to interchannel spatial misregistration effects.

The MIR radiance method is based on a power law approximation to the Planck function (Wooster *et al.*, 2003). The method exploits the fact that for the temperature range of active fires ($\sim 650 - 1350$ K) at MIR wavelengths the Planck function relationship between emitted spectral radiance and emitter temperature approaches a 4th order power law (Figure 5). Since the same fourth order power law is found in Stefan’s Law, which relates total energy radiated per second per unit area (i.e. over all wavelengths and over the hemisphere above the surface; so the Fire Radiative Power per unit area) to emitter temperature, the per unit area FRP can be expressed as a linear function of the fire emitted spectral radiance measured in a MIR spectral band (Wooster *et al.*, 2005):

$$FRP = \left(\frac{\sigma \cdot \epsilon_f}{a \cdot \epsilon_{f,MIR}} \right) L_{f,MIR} \quad [Wm^{-2}] \quad (3)$$

where σ is the Stefan-Boltzmann constant ($5.67 \times 10^{-8} \text{ W.m}^{-2}.\text{K}^4$), ϵ_f is the broadband emissivity of the fire and ϵ_{MIR} is the MIR spectral emissivity. Gray body behaviour is at

present assumed ($\epsilon_f = \epsilon_{f,MIR}$), which is understood to be a realistic approximation for vegetation fires (Langaas, 1995). $L_{f,MIR}$ ($\text{W} \cdot \text{m}^{-2} \cdot \text{sr}^{-1} \cdot \mu\text{m}^{-1}$) is the spectral radiance of the fire itself.

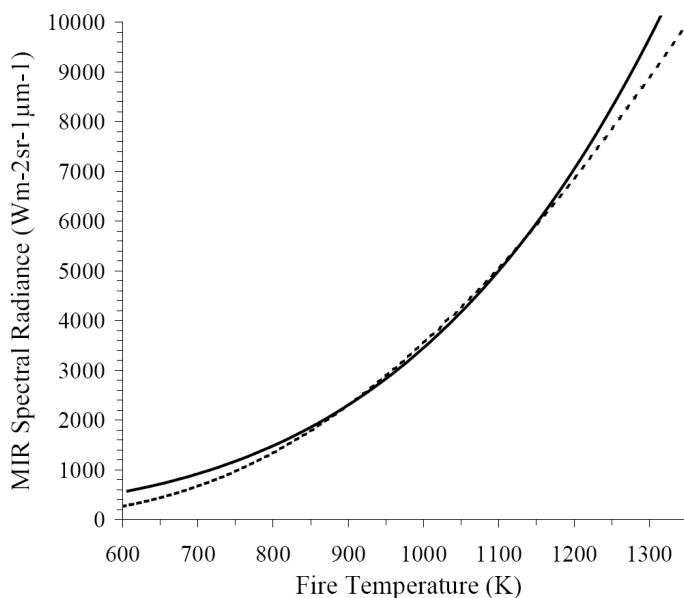


Figure 5. Spectral radiance at a MIR wavelength (3.7 μm) as derived from the Planck Function (solid line) and from a fourth order power law ($L = aT^4$; dashed line). For the range of emitter temperatures expected to encompass most of the temperatures seen in open vegetation fires (~650 – 1300 K) the power two relationships agree to within $\pm 12\%$.

With the coarse spatial resolution pixels of SLSTR, we cannot directly measure $L_{f,MIR}$ and can only measure the pixel integrated spectral radiance given by the mix of fire and ambient background (Equation 2). Thus $L_{f,MIR}$ is generally estimated as the difference between the MIR spectral radiance of the fire pixel and some average of the immediately surrounding non-fire ambient ‘background’ pixels. However, Equation (2) is a gross simplification that neglects many other contributions to the pixel radiance, so these must be included to obtain the full description of the fire pixel radiance to include both emissivity, atmospheric and solar radiation effects. Thus, for a pixel containing a sub-pixel sized fire, the at-sensor MIR spectral radiance (L_{MIR}) will be the summation the following terms; emitted fire thermal radiance, solar and atmospheric downwelling irradiance reflected from the fire, emitted thermal radiance from the non-fire background, the solar and downwelling atmospheric irradiance reflected from the non-fire background, and the upwelling atmospheric thermal radiation:

$$\begin{aligned}
 L_{MIR} = & \tau_{MIR} p_f \epsilon_{f,MIR} B(\lambda_{MIR}, T_f) + \tau_{MIR} p_f (1 - \epsilon_{f,MIR}) (\tau_{d,MIR} I_{sun,MIR} \cos \phi + I_{atm,MIR}) / \pi \\
 & + \tau_{MIR} (1 - p_f) \epsilon_{b,MIR} B(\lambda_{MIR}, T_b) + \tau_{MIR} (1 - p_f) (1 - \epsilon_{b,MIR}) (\tau_{d,MIR} I_{sun,MIR} \cos \phi + I_{atm,MIR}) / \pi \\
 & + L_{atm,MIR}
 \end{aligned} \quad (4)$$

where τ_{MIR} is the upward atmospheric transmission in the sensors MIR spectral channel, ϕ is the solar zenith angle, $\tau_{d,MIR}$ is the downward atmospheric transmission in the sensors MIR spectral channel at angle ϕ , $I_{sun,MIR}$ is the extraterrestrial solar irradiance in the sensors MIR spectral channel, $I_{atm,MIR}$ is the diffuse downwelling atmospheric irradiance in the MIR spectral channel, and $L_{atm,MIR}$ is the upwelling atmospheric spectral radiance in the MIR spectral channel. T is temperature, ϵ is emissivity and p the proportion of the pixel covered by that component, with subscript f corresponding to their value at the fire and b at the non-fire background.

Similarly for a neighbouring non-fire ‘background’ pixel:

$$L_{b,MIR} = \tau_{MIR} \epsilon_{b,MIR} B(\lambda_{MIR}, T_b) + \tau_{MIR} (1 - \epsilon_{b,MIR}) (\tau_{d,MIR} I_{sun,MIR} \cos \phi + I_{atm,MIR}) / \pi + L_{atm,MIR} \quad (5)$$

The fire emitted spectral radiance in the MIR spectral channel, $L_{f,MIR}$, required for input into equation (3) is in fact the $p_f \epsilon_{MIR} B(\lambda_{MIR}, T_f)$ term on the right hand side of equation (4), and its value can be obtained numerically by combining Equations (4) and (5) and re-arranging:

$$\begin{aligned}
 p_f \epsilon_{MIR} B(\lambda_{MIR}, T_f) = & \frac{1}{\tau_{MIR}} \left(L_{MIR} - (1 - p_f) L_{b,MIR} + p_f L_{atm,MIR} \right) \\
 & - p_f (1 - \epsilon_f) (\tau_{d,MIR} I_{sun,MIR} \cos \phi + I_{atm,MIR}) / \pi
 \end{aligned} \quad (6)$$

The rhs of Equation (6) represents the true value of $p_f \epsilon_{MIR} B(\lambda_{MIR}, T_f)$ for use as $L_{f,MIR}$ in Equation (3). Multiplying the output of (3) by the sensor ground field of view then provides an estimate of the fire radiative power in Watts.

However, certain of the parameters in Equation (6) cannot be readily determined, for example the unresolved fire fractional area, p_f , whilst others, for example the atmospheric parameters, are likely to be imperfectly known. By neglecting the (relatively) unimportant terms, Equation (6) can be greatly simplified and then parameterised using the SLSTR measured radiances, in order to provide an estimate of $L_{f,MIR}$ for input into Equation (3).

The first assumption is that the atmospheric term $p_f L_{atm,MIR}$ on the right hand side of Equation (6) will always be small compared to at least one of the first two terms and is therefore negligible. Next, the requirement to know the fire fractional area (p_f) is removed by assuming that $(1-p_f)L_{b,MIR} \approx L_{b,MIR}$, which is considered workable when p_f is sufficiently small, and as p_f increases the error this assumption introduces remains negligible since in that case the spectral radiance of the fire pixel will be increasingly dominated by emittance from the (increasingly large) fire rather than from the much cooler ambient background [since $B(\lambda_{MIR}, T_f)$ is many orders of magnitude larger than $B(\lambda_{MIR}, T_b)$ at MIR wavelengths; Figure 3]. The final term in Equation (6) corresponds to the solar and downwelling atmospheric radiation reflected from the fire, and is assumed negligible for the same reason.

Via these simplifications the fire-emitted spectral radiance ($L_{f,MIR}$) for input into Equation (3) can be estimated from the difference between the MIR spectral radiance of the active fire pixel (L_{MIR}) and that of the surrounding non-fire ‘background’ ($L_{b,MIR}$), which is generally estimated from the average signal of the valid (i.e. non-fire, non-water, non-cloud) pixels within a ‘background window’ surrounding the fire pixel. Thus:

$$L_{f,MIR} = p_f \epsilon_{f,MIR} B(\lambda_{MIR}, T_f) \square \frac{1}{\tau_{MIR}} (L_{MIR} - L_{b,MIR}) \quad (7)$$

Combining Equations (3) and (7) we obtain a method for calculating the FRP averaged over a coarse spatial resolution pixel in units of W.m^{-2} . Multiplying by the ground projection of the sensor FOV ($A_{sampler}$) provides the FRP in Watts:

$$FRP = \frac{1}{10^6 \cdot \tau_{MIR}} \left(\frac{\sigma \cdot \epsilon_f}{a \cdot \epsilon_{f,MIR}} \right) (L_{MIR} - L_{b,MIR}) \quad [\text{MW}] \quad (8)$$

3 ALGORITHM DESCRIPTION

3.1 Overview of Algorithm Structure

The SLSTR Active Fire algorithm can be considered a six-stage process, outlined in Figure 6. The stages are applied to SLSTR data that has already been cloud masked and separated into two subsets based on geographic location, namely the land area potentially capable of supporting land based hotspots (i.e. the land surface with the locations of larger lakes and rivers masked out) and the ocean areas that might potentially be the sites of ocean hotspots, i.e. offshore gas flares (i.e. this assumes that processing data of the entire open ocean would be computationally wasteful as is to be avoided where possible). The Sentinel-3 SLSTR channel naming convention and the matching scientific notation used throughout this document is shown in Appendix A. The algorithm is heavily reliant on data from the SLSTR 3.7 μm channel (bands S7 and F1) and 10.8 μm channel (bands S8 and F2). The precision of the measurements in the ‘standard’ bands (S7 and S8) is expected to be significantly better than that in the dedicated ‘fire’ channels (F1 and F2) and so where 3.7 μm and 10.8 μm measurements are used these should nominally be from the S7 and S8 channels unless measurement saturation is encountered, whereupon the corresponding measurement from the SLSTR F1 or F2 channel should be substituted instead. Note that the optical channels of the SLSTR are recorded at 500 m spatial resolution, whereas the thermal channels have a 1000 m spatial resolution. The SLSTR Active Fire algorithm uses data from both types of channel and this needs to be taken into account of during data processing where measurements from both types of channel are used (e.g. in a band ratio). Where the optical channels are used alone in a test it is desirable to undertake the analysis at the original 500 m spatial resolution, since the hotspot signals will be maximized at this smaller pixel area. Output from the product can, however, be delivered on a 1 km output grid.

The six fire detection stages utilize a series of spatially varying thresholds to detect the set of confirmed fire pixels in the scene under consideration, with the thresholds varying between day and night conditions. Furthermore, the thresholds vary between the detection of hotspots on land and over the ocean. Nighttime pixels are those defined as having a solar zenith angle $\geq 85^\circ$. By day, solar reflected radiation from cloud tops or edges can lead to high MIR signals at cloud-contaminated pixels, whereas the clouds will typically be cold and thus have

a low TIR signal. Therefore T_{MIR} , T_{TIR} and $\Delta T_{MIR-TIR}$ recorded at certain cloud-contaminated pixels maybe similar to those of fire pixels. Furthermore, inland water bodies (lakes and rivers), together with mixed land-water pixels at coastlines, can be expected to have rather different MIR and TIR brightness temperatures to the neighboring land surface pixels, and might also be affected by specularly reflected sunglint. Therefore the availability of an accurate cloud mask and land/water mask is very important for the fire application, and only SLSTR pixels that have been confirmed as clear-sky, land pixels via the use of such masks should be used within the land hotspot tests. Of course, some small or seasonally varying water bodies may not present in the land-water mask, and small or semi-transparent clouds may not be identified by the cloud mask. To assist in these instances the active fire detection algorithm contains some simple tests that aim to reduce problems introduced by such cases. A mask of “(semi-)permanent high temperature events” (e.g. land-based industrial heat sources, volcanoes) may also be applied after fire detection in order to separate such detections from true vegetation fires in terms of hotspot type classification.

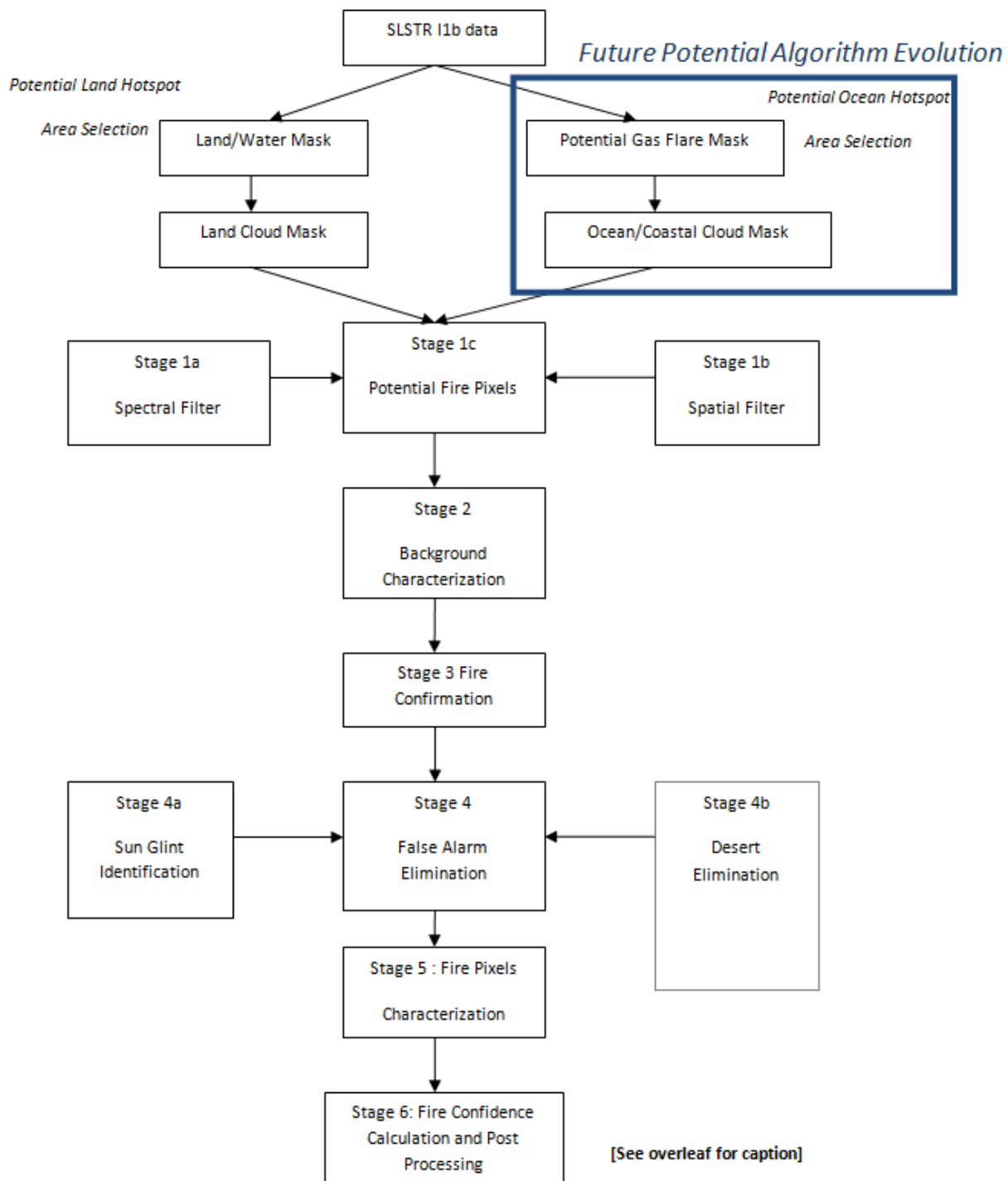


Figure 6 (prior page). Structure of the SLSTR Fire Detection and Characterisation algorithm.

Note: If the algorithm is evolved to include detection of offshore hotspots, prior to Stage 1 fire detection commencement, two separate geographic subsets of data would need to be determined, namely the cloud-free land area potentially capable of supporting land based hotspots (i.e. the land surface with the locations of clouds, larger lakes and rivers masked out) and cloud-free ocean areas that might potentially be the sites of offshore gas flares. Each of the stages is then applied to each of the two geographic subsets of data, though with some alterations to the thresholds used and in a few cases some tests being de-activated or added. The only exception is Stage 4b ‘desert elimination’ which is not necessary over the ocean. For both geographic subsets, thresholds and test details can vary between observations made under night-time and daytime conditions. Currently only the land area hotspot detection is implemented.

3.2 Detection of Potential Fire Pixels (Stage 1)

The purpose of this stage is to identify all pixels whose spectral and spatial signals suggest that they may potentially contain an actively burning vegetation fire. The aim is to successfully include all the true fire pixels within the potential fire pixel set, whilst minimizing the number of non-fire pixels included so as to minimize data processing overheads and avoid later false alarms. A spectral filter using set of spectral thresholds is applied to detect a set of potential fire pixels \mathcal{P}_s based on their NIR spectral reflectance, and thermal channel BT signals. In some circumstances, much of the cloud-free land surface maybe returned as a potential fire pixel by the spectral filter, particularly when thresholds are set low so as to minimize errors of omission (i.e. the missing of fire events). For this reason, a spatial (edge detection) filter is used to detect a second set of potential fire pixels \mathcal{P}_z based on the spatial variation of $\Delta T_{MIR-TIR}$, and the final set of potential fire pixels \mathcal{P}_f is based is the intersection of these two:

$$\mathcal{P}_f \in \{\mathcal{P}_1 \cap \mathcal{P}_2\} \quad (9)$$

Thus Stage 1c selects the final potential fire-pixel set as those pixels passing both Stages 1a and 1b. In the subsequent stages these pixels will then be further tested to confirm whether they do in fact contain an active fire. As with other stages, the processing is conducted independently for land and ocean geographic subsets, so two potential fire pixel sets are

ultimately produced, those corresponding to the land and those corresponding to the ocean respectively.

3.2.1 *Spectral Filter Detail (Stage 1a)*

Land Hotspots

Stage 1a identifies potential fire pixels belonging to set \mathcal{P}_i using two adaptive thresholds. Firstly, the scene is divided into equal sized sub-scenes having dimensions in terms of along- and across-track coordinates. The dimensions can be adapted with experience of real SLSTR data, but we suggest one half of the sensor swath width is used in the first instance. For each sub-scene being tested, the number of land (N_{land}) and cloud free land (N_{cf_land}) pixels is calculated. The subscene is classified as valid for use in adaptive threshold determination if the number of land pixels is greater than 10% of the total number of pixels in the subscene, and if the number of cloud free land pixels is greater than 1% of the total number of pixels in the subscene. In this case the mean values of T_{MIR} , T_{TIR} and $\Delta T_{MIR-TIR}$ for all cloud-free land pixels in that subscene are used as the spectral filter thresholds (\bar{T}_{MIR}^{cf} , \bar{T}_{TIR}^{cf} and $\bar{\Delta T}_{TIR-MIR}^{cf}$ respectively) against which each cloud-free land pixel in the subscene is tested for inclusion into potential fire pixel set \mathcal{P}_i :

$$T_{MIR} > \bar{T}_{MIR}^{cf} - 0.3\vartheta_s \quad (10a)$$

and

$$\Delta T_{MIR-TIR} > \bar{\Delta T}_{MIR-TIR}^{cf} \quad (10b)$$

and

$$T_{TIR} > \bar{T}_{TIR}^{cf} - 3K \quad (10c)$$

Where ϑ_s is the solar zenith angle (in degrees). Use of ϑ_s adjusts the MIR detection threshold

for the fact that at locations where the solar elevation is high, the ambient background temperature and the solar reflectance component of the MIR signal are typically greater.

Tests (10a) and (10b) are targeted at identifying the spectral signature of fires, whose pixel integrated MIR brightness temperature and MIR-TIR brightness temperature difference should in general be higher than those of the subscene ambient background. Using adaptive thresholds for the detection of potential fire pixels, rather than fixed thresholds such are used in the MODIS fire product (e.g. $T_{MIR} > 310$ K and $T_{MIR-TIR} > 10$ K; Giglio et al., 2003) provides the algorithm a chance at identifying the more weakly burning and/or smaller component of the fire regime – which can be rather numerous in areas such as disturbed tropical forests. The disadvantage is that many more non-fire pixels may also be returned, and Test (10c) is the initial test to try to minimize this effect, in this case by requiring any potential fire pixel returned by the spectral filter to be no more than 3 K cooler in the TIR channel than the mean of the subscene cloud free land pixels. Examination indicates that this test removes substantial numbers of potential fire pixels that are incorrectly detected by tests (10a) and (10b) at any areas of cloud edge that have missed being masked as cloud contaminated in any forerunning cloud masking operation.

If N_{land} and/or N_{cf_land} are too low to meet the 10% and 1% criteria specified above, then the weighted mean of the spatial filter thresholds \bar{T}_{MIR}^{cf} , \bar{T}_{TIR}^{cf} and $\bar{\Delta T}_{TIR-MIR}^{cf}$ calculated from the (maximum five) valid spatially neighboring subscenes are used (with the weighting for each subscene given by its value of N_{cf_land}). If no valid neighboring subscenes are available, which we expect to be relatively rare over most land areas given the non-stringent requirement for only 1% of land pixels to be cloud free, then default thresholds are used:

By day,

$$T_{MIR} > 310 \text{ K} - 0.3\theta_s \quad (10d)$$

and

$$\Delta T_{MIR-TIR} > 5 \text{ K} \quad (10e)$$

By night,

$$T_{MIR} > 290 \text{ K} \quad (10f)$$

and

$$\Delta T_{MIR-TIR} > 3 \text{ K} \quad (10g)$$

Pixels failing these preliminary tests are immediately classified as non-fire pixels. Pixels passing these tests belong to set \mathcal{P} relating to the land area.

3.2.2 *Spatial Filter Detail (Stage 1b)*

The spectral filter of Stage 1a is designed to be very liberal (in order to catch any possible fire pixels), with the disadvantage that it can return very large numbers of potential fire pixels many of which are not fires. Such pixels include those containing large areas of solar-heated bare rocks, soil or other “warm” surfaces, such as are found in arid or desert areas for example. In order minimize the inclusion of such areas in the final potential fire pixel set (\mathcal{P}) and so reduce potential commission errors and computational cost, a series of spatial thresholds is employed in conjunction with an edge detection filter. This test is used to identify locations where the $\Delta T_{MIR-TIR}$ signal shows a marked spatial change such as is found at fire pixels but not at areas of homogeneous warm land. A series of high-pass filters \mathbf{K} are applied to $\Delta T_{MIR-TIR}$ to identify a second potential fire pixel set \mathcal{P} [with, as before, one \mathcal{P} for land areas and one \mathcal{P} for ocean areas]. Since the contrast between fire and non-fire pixels is greater in $\Delta T_{MIR-TIR}$ than in the MIR channel alone, the spatial filter is applied to the brightness temperature difference data (Roberts and Wooster, 2008).

The idea behind the use of the high pass spatial filter is that since each SLSTR pixel measures the spatially averaged radiance over ~ 1 square kilometer, $\Delta T_{MIR-TIR}$ recorded at non-fire “background” pixels generally changes rather gradually from pixel to pixel. In contrast, a pixel containing an active fire represents a high spatial frequency change in $\Delta T_{MIR-TIR}$, which can thus be isolated via a high-pass spatial filter. Filter kernels of size $f_K \times f_K$ are used, where f_K is taken sequentially as 3, 5, 7 and 9, with the 3 x 3 filter having the coefficients shown in Figure 7.

-1	-1	-1
-1	8	-1
-1	-1	-1

Figure 7: Coefficients of the 3 x 3 high pass spatial filter.

Land Hotspots

The use of multiple filter kernel sizes attempts to ensure that the spatial filter is appropriate for detecting both single fire pixels and those belonging to larger spatial clusters of fire pixels. The edge detection filter is applied to the entire scene, and pixels passing the test are those where the filter output (h_K) exceeds a threshold defined in relation to the filter output standard deviation calculated from all the clear sky, land surface pixels in the SLSTR subscene within which the test pixel resides. A subscene has the same definition as in Stage 1a.

$$\mathcal{P}_2 \in \left\{ h_K \geq a_{sf} \sigma_{fK} \right\} \quad (11)$$

Where σ_{fK} is the standard deviation (Kelvin) of the clear sky, land surface pixels in the subscene, high-pass filtered with filter size f_K , and a_{sf} is the threshold multiplier taken as 1.5 currently. We use the same criteria for defining valid subscenes as per Stage 1a, and for calculation of the thresholds in the case that the current subscene under consideration fails to contain sufficient cloud free, land pixels. In the case where there are no valid subscenes available for a particular fire pixel (which is expected to be a rare occurrence), default values of σ_{fK} are used instead, notably 3, 10, 20 and 50 K for filter sizes of 3, 5, 7, and 9 pixels respectively.

A pixel having $\Delta T_{MIR-TIR}$ belongs to set \mathcal{P}_s if condition (11) is valid for at least one of the four filter kernel sizes f_K .

3.3 Background Characterisation (Stage 2)

The objective of the background characterization step is to provide an estimate of what the radiometric signal of the potential fire pixel would be in the absence of fire, based on statistics derived from the set of valid “background” pixels \mathcal{P}_b located within a window W of size $b_W \times b_W$ immediately surrounding the potential fire pixel being tested. Stage 3 will use this estimate to determine whether the observed potential fire pixel signal is sufficiently different to this value such that it can be confirmed as a true fire pixel.

Land Hotspots

At each potential land fire pixel belonging to set \mathcal{P}_f , b_W is initially set as 5. The center pixel of this 5 x 5 window is the potential fire pixel itself and so is discounted, and the immediately surrounding eight background pixels are also discounted since their closeness to the potential fire pixel can result in their radiances being contaminated by the fire radiance itself. Thus for the 5 x 5 sized window, a total of 16 pixels are initially included. From these 16 pixels, the set of valid background pixels \mathcal{P}_b are selected based on their being identified as clear-sky, land pixels that for daytime observations are not influenced by strong sun glint and which have:

$$T_{MIR,w} < T_{MIR,pf} \quad (12a)$$

$$\Delta T_{MIR-TIR,w} < \Delta T_{MIR-TIR,pf} \quad (12b)$$

$$T_{MIR,w} < 325 K \quad (12c)$$

$$\Delta T_{MIR-TIR,w} < 20 K \quad (12d)$$

$$\theta_g < 2^\circ \quad (12e)$$

Where $T_{MIR,w}$ and $\Delta T_{MIR-TIR,w}$ is middle infrared brightness temperature and brightness temperature difference of the pixel in the background window respectively; $T_{MIR,pf}$ and $\Delta T_{MIR-TIR,pf}$ is middle infrared brightness temperature of the potential fire, θ_g is sun glint

angle. The purpose of tests 12a-12e is, as far as possible, to remove other fire pixels from the background pixel set and to thus select \mathcal{P}_b as being representative of the uncontaminated ambient background signal. For nighttime observations the sunglint test is not required and the thresholds for test 12c and 12d are lowered to 310 K and 10 K respectively.

If the number of valid background pixels in set \mathcal{P}_b is greater than 25% of the total number of background pixels (excluding from the total number of background pixels the potential fire pixel itself and the 8 immediate surrounding pixels; so 16 pixels for the smallest b_W of 5) [and for the smallest b_W of 5 the total number of pixels is eight or more] then the background window statistical characterization process proceeds immediately using a window size b_W of 5. If this condition is not met, the window size b_W is increased through 7, 9, 11, 13, 15, 17, 19 and 21 and the test repeated at each stage until the conditions are met. For each window size the 8 pixels spatially neighboring the potential fire pixel itself (along with the potential fire pixel being tested and any other potential fire pixels within the window) are excluded from the background pixel set, and thus for example the maximum number of background pixels in the case where $b_W = 7$ is 40 (7*7-9).

If an insufficient number of valid neighboring pixels is identified using even the 21 x 21 window, the background characterization is unsuccessful and the fire pixel is classed as “unknown”. The approach inherently assumes that the spatially closest pixels to the potential fire pixel being tested have a signal most similar to that which the potential fire pixel would have in the absence of fire. The 21x 21 background window maximum size, though somewhat arbitrary, ensures that the background signal is sampled within ~ 11 km of the potential fire pixel location, a scale that (Giglio *et al.*, 2003) found empirically to be appropriate for preventing false alarms induced by the unrepresentative selection of background pixels.

Following Giglio *et al.* (2003) the number of valid background pixels within the background window is recorded as N_b . The number of pixels excluded from the background window is also recorded for later use in false alarm reduction and in defining the fire pixel confidence measure. The number of pixels (N_f) excluded as being “background fires” is set as the total number failing test 12c and test 12d, and the number excluded as being water/land pixels (in

the land/ocean hotspot testing respectively) or cloud-contaminated pixels is recorded as $N_{w/l}$ and N_c respectively.

For each potential fire pixel where a sufficient number of valid background pixels are identified (which is the vast majority of cases), the background characterisation is classed as successful and a number statistical measures computed from the valid background pixel set \mathcal{P}

b. These are \bar{T}_{MIR} and σ_{MIR} , the respective mean and mean absolute deviation of T_{MIR} ; \bar{T}_{TIR} and σ_{TIR} , the respective mean and mean absolute deviation of T_{TIR} ; $\bar{\Delta T}_{MIR-TIR}$ and $\sigma_{\Delta T_{MIR-TIR}}$, the respective mean and mean absolute deviation of $\Delta T_{MIR-TIR}$, and $\bar{R}_{RED/MIR}$ the mean ratio of the MIR and RED (0.86) radiance calculated over the valid background pixel set. Again following Giglio *et al.* (2003) the MIR brightness temperature mean and mean absolute deviation of those spatially neighboring pixels that were rejected as background fires by test 12c and test 12d are also computed and denoted as \bar{T}_{MIR}' and σ_{MIR}' , respectively, since they can prove useful for rejecting certain ‘warm surface’ false alarms. As suggested by Giglio *et al.* (1999), we employ the mean absolute deviation here as a measure of dispersion, rather than the standard deviation, since it is more resistant to outliers (Huber, 1981). For contextual fire detection algorithms, this is a highly desirable feature since as far as possible we wish to avoid contamination of the background window statistics by pixels containing cloud, water, or fire that have not been correctly identified as such.

3.4 Fire Pixel Confirmation (Stage 3)

This stage uses the statistics from the potential fire pixel and the matching background window to confirm whether or not the potential fire pixel actually contains an active fire. An absolute threshold and a series of contextual thresholds, varied on the basis of the background window statistics, are employed.

3.4.1 Absolute Threshold Test (Stage 3a)

Prior to the series of contextual tests, an absolute threshold test is used to identify the most radiant fire pixels in a scene. Such a test may be required for example if a high intensity fire pixel is located within a very large cluster of surrounding fire pixels, from which it has

proven impossible to gain a sufficient number of valid background window pixels, or where the background window statistics have for some reason become contaminated by radiance from the immediately surrounding fires. We use the absolute threshold test initially used by Kaufman *et al.* (1998) and still used within the MODIS fire detection algorithm. For daytime pixels a potential fire pixel is confirmed as a true fire pixel (even if at Stage 2 it was classed as “unknown”) if:

$$T_{MIR} > 360 \text{ K} \quad \text{by day} \quad (13a)$$

$$T_{MIR} > 320 \text{ K} \quad \text{by night} \quad (13b)$$

These thresholds are chosen on the basis that no ambient non-fire pixels are expected to attain these high brightness temperature due to thermal emission and daytime near lambertian reflection of MIR wavelength solar radiation. However, as Giglio *et al.* (2003) points out, despite the high daytime threshold, by day the use of this test must be accompanied by adequate sun glint rejection, otherwise sunglint false alarms may occur.

In addition, since at night signals from the S6 channel (SWIR2; 2.25 μm) should essentially be zero over ambient temperature surfaces, but fires emit significantly at this wavelength (Figure 3) then where available the signal in this channel can be used to detect nighttime fires that might be missed by the tests based on fires signal in the MIR and TIR channel signals alone. This is especially the case since the pixel size of these SLSTR optical channels is 500 m, as opposed to 1 km for the thermal channels, so any fire should comprise a higher proportion of the S6 pixel area. An additional absolute threshold test is therefore used to make use of this capability.

$$L_{SWIR2} > \bar{L}_{SWIR2} + n_{SWIR2} \quad \text{by night} \quad (13c)$$

Where L_{SWIR_2} is the spectral radiance recorded in the S6 channel ($\text{W}\cdot\text{m}^{-2}\cdot\text{sr}^{-1}\cdot\mu\text{m}^{-1}$), \bar{L}_{SWIR_2} is the mean spectral radiance signal determined from the S6 channels at night over ambient cloud free land in the scene defined in Section 3.2, and n_{SWIR_2} is a value determined from the S6 channel noise level (expected to be the measured noise level multiplied by a scaling factor, such as 2.5). The definition of “night” here may be required to be different than that used in the prior-stages of the algorithm, depending on reflected sunlight levels at high solar zenith angles.

Equivalents to Test 13c are not available by day, since the high solar reflected signal at these SWIR wavelengths will swamp all but the largest/most extreme fire signals. Such fires would in any case be picked up by the other MIR channel based tests, and using the S6 (or S5) channel by day could likely simply increase false alarm rate.

Since fire pixels detected with the absolute threshold test do not require background characterization values, it is possible to have fires detected by this test even when the background characterization process fails. However, in such a case the FRP of the fire pixel would not be able to be estimated since there would be no background MIR radiance value to use in Equation 19. Therefore, in the rare cases where this occurs, the background window should continue to be expanded beyond 21 x 21 pixels to a maximum of 50 x 50 pixels until at least 50 background pixels are available to perform the background characterization process and thus estimate FRP. Since all fire pixels detected by the absolute threshold tests will by definition be very large fires, the fact that the background statistics in these cases will come from areas further away from the fire pixel than normal (and so maybe less representative of the fire pixel background itself) is less important than at lower FRP fire pixels due to the very large MIR fire signals involved (i.e. in Equation 19; $L_{f,MIR} \gg L_{b,MIR}$). If even with the 50 x 50 pixel window upper limit there remain insufficient background pixels to meet the 50 pixel criteria, which is expected to be a very rare occurrence, then the FRP should be estimated with $L_{b,MIR}$ taken as the mean of the non-cloud, non-sunglint pixels of the sub-scene pixels having the same land/ocean classification as the fire pixel itself, and with the absolute uncertainty (δ_{L_b}) in the estimate of the fire pixel background radiance [used in Equation (19)] taken as that equivalent to a ±10 K uncertainty in the equivalent brightness temperature.

The same absolute threshold tests are used for land and ocean hotspots if the latter is eventually implemented.

3.4.2 *Contextual Threshold Tests (Stage 3b)*

Land Hotspots

For potential fire pixels from the set \mathcal{P}_f corresponding to land hotspots and where the background characterization was successful but the potential fire pixel T_{MIR} was not high enough to pass the absolute threshold test (13a or 13b), a series of contextual threshold tests are used to test confirmation of the potential fire pixel. These tests examine the T_{MIR} , T_{TIR} and $T_{MIR-TIR}$ potential fire pixel signals and compare these to the mean signals from the background window, with the exact thresholds adjusted to take into account the variability of the background window as measured by the mean absolute deviation. The contextual tests employed are:

$$L_{RED/MIR} > \bar{L}_{RED/MIR} \quad (14a)$$

$$\Delta T_{MIR-TIR} > \Delta \bar{T}_{MIR-TIR} + 3.2\sigma_{\Delta T_{MIR-TIR}} \quad (14b)$$

$$\Delta T_{MIR-TIR} > \Delta \bar{T}_{MIR-TIR} + 5.6K \quad (14c)$$

$$T_{MIR} > \bar{T}_{MIR} + 3\sigma_{T_{MIR}} \quad (14d)$$

$$T_{TIR} > \bar{T}_{TIR} - 4K \quad (14e)$$

$$\sigma'_{MIR} > 5K \quad (14f)$$

These tests are based on those in Giglio *et al.* (2003), but adapted for SLSTR because of its wideband 3.7μm MIR channel, rather than the narrowband MODIS 3.9 um channel for which the tests were originally designed. Test (14a) has been added to help in the removal of potential fire pixels caused by sunglints, since at such pixels both RED and MIR radiances will be increased whereas at fire pixels only the MIR will be.

Where $R_{RED/MIR}$ is the ratio between the MIR radiance and RED radiance of the potential fire pixel and $\bar{R}_{RED/MIR}$ is the mean ratio between the MIR radiance and RED radiance of the valid background pixels.

σ'_{MIR} is the standard deviation of the “background fires” identified using tests 12c and 12d. It is used to reject potential fire pixels caused by hot desert areas as typically this value will be low there due to the uniformly warm surface extending over many pixels.

A daytime potential land fire pixel from \mathcal{P}_f will be classified as a confirmed fire pixel if:

{The absolute threshold test (13a) is true}

or

{Tests (14a) – (14d) are true and [test (14e) or test (14f) is true]},

otherwise it is classified as a non-fire pixel.

A nighttime potential land fire pixel from \mathcal{P}_f is classified as a true fire pixel if:

{The absolute threshold Test 13b is true; or Tests 13c or 13d are true}

or

{Tests (14b) – (14d) are true},

otherwise it is classified as a non-fire pixel

At pixels for which the background characterization failed, i.e. due to an insufficient number of valid background pixels being identified in the background window, only Tests 13a to 13d can be applied. In this case if any of Tests 13a to 13d are true then the pixel is classified as a fire pixel, otherwise the pixel is classified as “unknown”.

3.5 False Alarm Elimination (Stage 4)

Locations having a radiometrically strong spatial contrast across a geographic boundary in the MIR and TIR channels can potentially cause either errors of omission or commission for a contextual detection algorithm. Sunglint and desert boundaries are two of the most common features to induce such false alarms.

3.5.1 Sun Glint Identification (Stage 4a)

By day, sun glint over small-unmasked water bodies or cloud, or even from areas of wet or sometimes bare soil, can increase the MIR pixel signal considerably above the TIR signal and lead to false alarms. Such instances are rejected using a scheme based on a combination of those in Giglio (2003) and Zhukov *et al.* (2006), using the glint angle (θ_g) calculated between the sensors viewing direction and the direction of the suns rays specularly reflected from the horizontal (usually water) surface:

$$\theta_g = \cos \theta_v \cos \theta_s - \sin \theta_v \sin \theta_s \cos \theta_\phi \quad (15)$$

Where, θ_v and θ_s are the view and solar zenith angles respectively, and θ_ϕ is the relative azimuth angle between them.

The following conditions are then evaluated:

$$\theta_g < 2^\circ \quad (16a)$$

$$\rho_{RED} > 0.15 \quad (16b)$$

$$\theta_g < 8^\circ \text{ and } L_{MIR} / L_{RED} < 0.008 \quad (16c)$$

Tests 16a and 16b reject as false alarms all fire pixels in the strongest region of glint based on a small glint angle, or which have very high RED reflectance. Test 16c also rejects fire pixels in the less intense glint region but which show an insufficiently large ratio of MIR to RED radiance (since only the MIR channel signal will be increased substantially by a fire, whereas both will be increased by glint).

The same strategy for glint identification is used for land and oceanic hotspots.

3.5.2 *Desert Boundary Rejection (Stage 4b)*

For the land surface geographic region, spatial boundaries between surfaces of significantly different ambient temperatures can pose problems, since the pixels on the hotter side of the boundary can sometimes be excluded from the background window tests in Stage 2, leading to cooler background window statistics and the possibility that the hotter land surface pixels may then be falsely identified as fire pixels. We use the method of Giglio *et al.* (2003) to reject such falsely detected fire pixels, using the statistics T'_{MIR} and σ'_{MIR} calculated in Stage 2, along with a series of spectral thresholds. During the daytime most desert areas that might lead to such false alarms are expected to have a high and relatively uniform surface temperature, with T'_{MIR} is expected to be around 335 K, and σ'_{MIR} around 0.5 K. For a background containing highly radiating fire pixels, however, σ'_{MIR} will be much larger (perhaps 40 K or above), and T'_4 will be somewhat larger, at maybe 350 – 380 K. Tests 17a–17f from Giglio *et al.* (2003) exploit these characteristics as a means of rejecting daytime false alarms arising along “desert boundaries”:

$$N_f > 0.1N_v \quad (17a)$$

$$N_f > 4 \quad (17b)$$

$$\rho_{NIR} > 0.15 \quad (17c)$$

$$T'_{MIR} < 345K \quad (17d)$$

$$\sigma'_{MIR} < 3K \quad (17e)$$

$$T_{MIR} < T'_{MIR} + 6\sigma'_{MIR} \quad (17f)$$

If all the above tests are satisfied, the fire pixel is rejected as a false alarm caused by a hot desert boundary. This test is only applied to the land surface geographic area, and not the oceanic area.

3.6 Fire Characterisation (Stage 5)

At each confirmed fire pixel having a valid number of background pixels, the FRP is calculated as:

$$FRP = \frac{A_{sampler}}{10^6 \tau_{MIR}} \left(\frac{\sigma}{a} \right) (L_{MIR} - \bar{L}_{MIR}) \quad [\text{MW}] \quad (18)$$

Where $A_{sampler}$ is the ground projection area of the sensor FOV (in m^2), which generally varies with viewing angle. σ is the Stefan-Boltzmann constant ($5.67 \times 10^{-8} \text{ W} \cdot \text{m}^{-2} \cdot \text{K}^{-4}$), L_{MIR} is the spectral radiance of the fire pixel in the MIR channel ($\text{W} \cdot \text{m}^{-2} \cdot \text{sr}^{-1} \cdot \mu\text{m}^{-1}$) and \bar{L}_{MIR} is the mean spectral radiance of the valid background window pixels in the MIR channel ($\text{W} \cdot \text{m}^{-2} \cdot \text{sr}^{-1} \cdot \mu\text{m}^{-1}$), and a is the constant from the power-law linking radiance to 4th power of emitter temperature ($\text{W} \cdot \text{m}^{-2} \cdot \text{sr}^{-1} \cdot \mu\text{m}^{-1} \cdot \text{K}^{-4}$; see Section 2.4.2). The actual value of a will depend on the exact spectral response function of the SLSTR MIR spectral band – but at present a value of $3.327 \times 10^{-9} \text{ W} \cdot \text{m}^{-2} \cdot \text{sr}^{-1} \cdot \mu\text{m}^{-1} \cdot \text{K}^{-4}$ can be used. The division by 10^6 converts the FRP into units of MW.

4 UNCERTAINTY BUDGET

4.1 FRP Error Estimation and Fire Pixel Confidence Assessment (Stage 6)

4.1.1 FRP Error Estimation

The estimation of FRP in Equation (18) is subject to random errors resulting from uncertainties in the value of a and τ_{MIR} , and in the assessment of $L_{f,MIR}$ and $L_{b,MIR}$.

Assuming that these are uncorrelated, the corresponding uncertainty (δ_{FRP} ; MW) in FRP is:

$$\delta_{FRP} = FRP \sqrt{\left(\frac{\delta_a}{a}\right)^2 + \left(\frac{\delta_\tau}{\tau}\right)^2 + \left(\frac{\delta_{L_f}}{L_f - L_b}\right)^2 + \left(\frac{\delta_{L_b}}{L_f - L_b}\right)^2} \quad [\text{MW}]$$

(19)

Where δ_a is the absolute error (in MW) resulting from the power law approximation to the Planck function used in deriving Equation (18). Assuming a fire temperature range of 675 to 1300K the value of $\frac{\delta_a}{a}$ is about 0.1 at one sigma (Wooster *et al.*, 2005)

δ_τ is the absolute error in the estimation of atmospheric transmission in the MIR channel (as used in Equation 18).

δ_{L_f} is the absolute uncertainty of the fire pixel radiance measure ($\text{W.m}^{-2}.\text{sr}^{-1}.\mu\text{m}^{-1}$), derived from the noise statistics of the SLSTR MIR channel

δ_{L_b} is the absolute uncertainty in the estimate of the fire pixel background radiance ($\text{W.m}^{-2}.\text{sr}^{-1}.\mu\text{m}^{-1}$), taken as the standard deviation of the MIR channel radiance measures of the valid background window pixels.

4.1.2 Fire Pixel Confidence Assessment

Fire pixel errors of omission and commission are always present in the results of any active fire detection algorithm. There is an inherent tradeoff as it is possible to reduce errors of commission (i.e. false alarms) to zero by having an extremely conservative fire detection algorithm with very strict thresholds. The downside of this approach is that errors of omission will be very high – and most true fire pixels maybe missed. In the SLSTR algorithm we have instead attempted to minimise the occurrence of false alarms via an optimised contextual fire detection scheme whose principles are based on forerunner algorithms that have shown strong levels of performance levels when applied to MODIS polar orbiting and SEVIRI geostationary datasets. Nevertheless, errors of commission with these prior schemes are noted to be of the order of 5 to 10%, and so a similar commission error is expected with SLSTR, certainly until more experience is gained with the data and the algorithm can be

tuned or modified accordingly. This is especially true since we currently do not know the performance level of the cloud detection scheme upon which the fire detection algorithm depends.

Since errors of commission are certainly going to be present in the output dataset, a measure of detection confidence for each confirmed fire pixel is ideally required, such that users can opt to utilise only certain high confidence active fire detections for example. The scheme for deriving the confidence measure is based on the approach of Giglio et al. (2003), and which has also been adopted for the SEVIRI FRP product (Wooster and Roberts, 2008). Detection confidence is defined according to a combination of the absolute and relative fire-pixel signal, and to the number of near-neighbouring cloud and water pixels (the idea here being that fire pixels detected close to such features are more likely to be false detections due to sunglint or other non-fire effects (e.g. a strong thermal contrast across a geographic boundary; coupled with interchannel spatial misregistration between the TIR and MIR bands). The confidence measure employs T_{MIR} , N_w , N_c , and the standardized variables Z_{MIR} and $Z_{\Delta T_{MIR-TIR}}$, which are defined as:

$$Z_{MIR} = \frac{T_{MIR} - \bar{T}_{MIR}}{\sigma_{MIR}} \quad (20)$$

$$Z_{\Delta T_{MIR-TIR}} = \frac{\Delta T_{MIR-TIR} - \bar{\Delta T}_{MIR-TIR}}{\sigma_{\Delta T_{MIR-TIR}}} \quad (21)$$

These quantities represent the number of absolute deviations that T_{MIR} and $\Delta T_{MIR-TIR}$ lie above the background, and are analogous to the more commonly used Z-scores that are calculated using the standard deviation. A ramp function is defined as:

$$S(\chi; \alpha, \beta) = \begin{cases} 0; & \chi \leq \alpha \\ (\chi - \alpha)/(\chi - \beta); & \alpha < \chi < \beta \\ 1; & \chi \geq \beta \end{cases} \quad (22)$$

The confidence assigned to each fire pixel is composed of a combination of five sub-confidences, labelled C₁ to C₅, each having a range of 0 (lowest confidence) to 1 (highest confidence). For daytime fire pixels, these are defined as

$$C_1 = S(T_{MIR}; 310K, 340K) \quad (23)$$

$$C_2 = S(Z_{MIR}; 2.5, 6) \quad (24)$$

$$C_3 = S(Z_{\Delta T_{MIR-TIR}}; 3, 6) \quad (25)$$

$$C_4 = 1 - S(N_c; 0, 6) \quad (26)$$

$$C_5 = 1 - S(N_w; 0, 6) \quad (27)$$

For C₁, 310 K represents a brightness temperature that is likely to be towards the minimum brightness temperature required for a pixel to be considered a fire pixel (and is thus less obviously a fire), while based on experience, 340 K represents a typical value for a reasonably obvious fire. For C₂, Z_{MIR} = 2.5 is the minimum value required of fire pixels by the detection algorithm, whereas Z_{MIR} = 6 represents a typical value (again based on experience) for an unambiguous fire. A similar rationale applies to the definition of C₃. C₄ reduces the detection confidence as the number of adjacent cloud pixels increases, accounting for the fact that fire pixels detected along cloud edges are more likely to suffer from cloud contamination, potentially triggering a false alarm via reflected sunlight. Finally, C₅ reduces the confidence as the number of adjacent water pixels increases, reflecting the greater likelihood that the detected fire pixel is instead a false alarm induced by a coastal boundary.

Following Giglio et al. (2003), the detection confidence of the fire pixel C is then defined as the geometric mean of the sub confidences, i.e.

$$C = \sqrt[5]{C_1 C_2 C_3 C_4 C_5} \quad (28)$$

For nighttime fire pixels, the thresholds of C₁ are altered so that

$$C_1 = S(T_4; 305K, 320K) \quad (29)$$

The others remain the same as for daytime imagery.

In the case where a fire pixel has been detected with the absolute threshold the fire confidence parameter C is automatically set to 1.

5 PRACTICAL CONSIDERATIONS

5.1 Cloud masking

Cloud masking is essential to the fire product due to the fact that optically thick clouds make it impossible to identify active fires through passive remote sensing, and solar reflected MIR radiation from certain clouds can appear similar to fire signals. Thus, some cloud-contaminated pixels will likely be falsely classified as fires if they are not masked out prior to fire detection.

However, it is also the case that some cloud masking algorithms use tests (e.g. those based on thermal channel differences) that can erroneously identify fire-related hotspot pixels as cloud. Furthermore, some cloud mask algorithms also identify optically thick smoke as cloud, even though fire detections can typically be made through smoke since it is relatively transparent at MIR wavelengths (unlike meteorological cloud). Therefore care should be taken in the deployment of the generic SLSTR cloud mask with regard to its use in masking the SLSTR observations prior to Stage 1 of the fire detection algorithm (Figure 6), and it is possible that only some of the cloud masking tests will be relevant to masking data prior to application of the fire detection and characterization algorithm.

To try to ensure that the cloud mask available for SLSTR is of maximum relevance to the fire product, over the land it can potentially be enhanced or even replaced by a further simple mask developed for the fire product based on the following simple tests taken from Giglio *et al.* (2003b):

$$\{(\rho_{\text{RED}} + \rho_{\text{NIR}} > 0.9) \text{ or } T_{\text{TIR2}} < 265 \text{ K}\}$$

or

$$\{ (\rho_{\text{RED}} + \rho_{\text{NIR}} > 0.7) \text{ and } T_{\text{TIR2}} < 285 \text{ K}\}$$

Similar tests, with adjusted thresholds, could also be applied over ocean areas.

5.2 Water masking

Given the contextual nature of the algorithm, when analyzing potential land fire pixels it is important to accurately exclude water and mixed water pixels during the background characterization stage. Such pixels are usually cooler than adjacent land pixels during the day. Unknowingly including water and mixed land-water pixels in the background window can depress T_4 and cause false alarms. Also contributing to this phenomenon is the fact that compared to land, water pixels frequently have lower values of $\Delta T_{MIR-TIR}$ due to differences in emissivity. Water and mixed land-water pixels contaminating the background window can therefore decrease $\Delta \bar{T}_{MIR-TIR}$ and thus increase the likelihood that a false alarm will occur. Therefore prior to the algorithm application a set of tests is used in daytime areas to identify water contaminated pixels that have not been masked out by the land-water mask. Following Giglio et al. (2003), we use a simple test based on the 0.86 μm and 2.1 μm reflectances and the Normalized Difference Vegetation Index (NDVI) of the valid background pixels, where $\text{NDVI} = (\rho_{NIR} - \rho_{RED}) / (\rho_{NIR} + \rho_{RED})$. This particular combination was chosen to reduce the likelihood of confusing cloud shadows and burn scars, which also have low surface reflectance, with water. Valid background pixels having $\rho_{SWIR2} < 0.05$ and $\rho_{NIR} < 0.15$ and an $\text{NDVI} < 0$ are considered to be water pixels. The number of such pixels is denoted as N_{uw} . If the absolute threshold test (Section 3.2.3) is not satisfied and $N_{uw} > 0$, the tentative fire pixel is rejected and classified as non-fire, otherwise it is classified as fire.

6 EVOLUTION

Currently the algorithm is designed only to detect and characterize hotspots on the land surface. The next stage of the algorithms evolution would likely be to include the potential to perform analysis on offshore hotspots (e.g. gas flaring from oil and gas rigs) as well. A mask to identify the location of possible offshore hotspots (i.e. a coastal buffer around potential offshore gas flaring locations) would be required for this task, as well as the following additions to the different algorithm stages.

Stage 1a

Ocean Hotspots

Similar to Stage 1a for the land hotspots, the task of Stage 1a here is to highlight potential hotspots (i.e. gas flares) in ocean areas. However, since the potential geographic area for flares to occur in is relatively small, and the oceanic background is much more homogeneous than the land, the region is not subdivided as it was for the land hotspot detection Stage 1a. Firstly, the number of cloud free pixels within the geographic ocean mask window is calculated (N_{cf_ocean}). If this is greater than a pre-determined threshold (currently set at 2000 pixels) the scene will be treated as valid for potential gas flare detection and will be processed for Stage 1a.

In this case the mean values of T_{MIR} , T_{TIR} , and $\Delta T_{MIR-TIR}$, L_{swir1} and L_{SWIR2} for all cloud-free ocean pixels in the scene are used as the respective spectral filter thresholds (\bar{T}_{MIR}^{cf} , \bar{T}_{TIR}^{cf} , $\bar{\Delta T}_{TIR-MIR}^{cf}$, \bar{L}_{SWIR1}^{cf} and \bar{L}_{SWIR2}^{cf}) against which each cloud-free ocean pixel in the scene is tested for inclusion into the potential fire pixel set \mathcal{P} relevant to the potential ocean hotspot area. Here L_{SWIR1} and L_{SWIR2} are the radiances in the SLSTR S5 and S6 bands respectively and the other terms have the meanings already described.

Over the ocean, in addition to Tests 10a to 10c, two further tests are employed:

$$L_{SWIR1}^{pf} > \bar{L}_{SWIR1}^{cf} \quad (10h)$$

and

$$L_{SWIR2}^{pf} > \bar{L}_{SWIR2}^{cf} \quad (10i)$$

If N_{cf_ocean} is too low to meet the pre-determined threshold criteria specified above, then default thresholds are used:

By day:

$$\begin{aligned} T_{MIR} &> 295 \text{ K} & (10d' \text{ where } ' \text{ indicates a variation on the original test} \\ & 12c) \end{aligned}$$

and

$$\Delta T_{MIR-TIR} > 1 \text{ K} \quad (10e')$$

By night,

$$T_{MIR} > 285 \text{ K} \quad (10f')$$

and

$$\Delta T_{MIR-TIR} > 0.5 \text{ K} \quad (10g')$$

Pixels failing these preliminary tests are immediately classified as non-fire pixels. Pixels passing these tests belong to set \mathcal{P}_i relating to the potential ocean hotspot area.

Stage 1b

Ocean Hotspots

A similar approach is used for ocean areas as for the land areas, though again instead of using subscenes, the entire potential ocean hotspot area within the scene is used as one. The edge

detection filter is applied to the potential ocean hotspot area, and pixels passing the test are those where the filter output (h_K) exceeds a threshold defined in relation to the filter output standard deviation calculated from all the clear sky, ocean pixels in the potential ocean hotspot area (Equation 11). In the case where there is an insufficient number of pixels (currently < 2000 pixels) in the potential ocean hotspots area for the determination of σ_{fK} for a particular fire pixel (which is expected to be a rare occurrence), default values of σ_{fK} are used instead, notably 1, 3, 6 and 10 K for filter sizes of 3, 5, 7, and 9 pixels respectively. As with other absolute thresholds used herein, these maybe adapted with experience of real SLSTR data.

Stage 2

Ocean Hotspots

Similar to the land, at each potential fire pixel belonging to set \mathcal{P}_f relevant to the ocean areas, b_w is initially set as 5. The center pixel of this 5 x 5 window is the potential fire pixel itself and so is discounted, and the immediately surrounding eight background pixels are also discounted since their closeness to the potential fire pixel can result in their radiances being contaminated by the fire radiance itself. Thus for the 5 x 5 sized window, a total of 16 pixels are initially included as potential valid pixels for the background characterisation. From these 16 pixels, the set of valid background pixels \mathcal{P}_b are selected based on their being identified as clear-sky, ocean pixels that for daytime observations are not influenced by strong sun glint and which should passed following tests in addition to Test 12a, 12b and 12 e :

$$T_{MIR,w} < 315 \text{ K} \quad (12c' \text{ where } ' \text{ indicates a variation on the original test 12c})$$

$$\Delta T_{MIR-TIR,w} < 10 \text{ K} \quad (12d')$$

$$L_{SWIR1,w} < L_{SWIR1,pf} \quad (12f)$$

$$L_{SWIR2,w} < L_{SWIR2,pf} \quad (12g)$$

Where $L_{SWIR1,w}$ and $L_{SWIR2,w}$ are radiance recorded in bands S5 and S6 of the background window pixel under consideration, and $L_{SWIR1,pf}$ and $L_{SWIR2,pf}$ are the radiances of the potential fire pixel in S5 and S6. For nighttime observations the sunglint test is not required and the thresholds for Test 12c' and 12d' are lowered to 305 K and 5 K respectively.

In the same way as for the land hotspot tests, if at least 25% of the background window pixels (which are $b_w \times b_w$ in number) are deemed valid, and their absolute number is 8 or more, then the background window statistical characterization process proceeds immediately using a window size b_w of 5. If either of these conditions are not met, the window size b_w is increased through 7, 9, 11, 13, 15, 17, 19 and 21 as for the land hotspot case.

Following Giglio *et al.* (2003) the number of valid background pixels within the background window is recorded as N_b . The number of pixels excluded from the background window is also recorded for later use in false alarm reduction and in defining the fire pixel confidence measure. The number of pixels (N_f) excluded as being “background fires” is set as the total number failing test 12c' and test 12d'. The number excluded as being land pixels or cloud-contaminated pixels is recorded as $N_{w/l}$ and N_c respectively.

For each potential fire pixel where a sufficient number of valid background pixels are identified (which is the vast majority of cases), the background characterisation is classed as successful and a number statistical measures computed from the valid background pixel set \mathcal{P}_b relating to the potential ocean hotspot area. These are \bar{T}_{MIR} and σT_{MIR} , the respective mean and mean absolute deviation of T_{MIR} ; \bar{L}_{MIR} and σL_{MIR} , the respective mean and mean absolute deviation of L_{MIR} ; \bar{T}_{TIR} and σT_{TIR} , the respective mean and mean absolute deviation of T_{TIR} ; $\bar{\Delta T}_{MIR-TIR}$ and $\sigma_{\Delta T_{MIR-TIR}}$, the respective mean and mean absolute deviation of $\Delta T_{MIR-TIR}$ and $\bar{R}_{RED/MIR}$ the mean ratio of the MIR and RED radiance calculated over the valid background pixel set; $\bar{\rho}_{red}$ and $\sigma \rho_{red}$, the mean and mean absolute deviation of ρ_{red} (Band S3); \bar{L}_{SWIR1} and σL_{SWIR1} , the mean and mean absolute deviation of L_{SWIR1} (Band S5); \bar{L}_{SWIR2} and σL_{SWIR2} , the mean and mean absolute deviation of L_{SWIR2} (Band S6). The MIR brightness temperature mean and mean absolute deviation of those spatially neighboring pixels that were

rejected as background fires by test 12c and test 12d are also computed and denoted as \bar{T}_{MIR}' and σ_{MIR}' , respectively.

Stage 3b

Ocean Hotspots

For potential fire pixels from the set \mathcal{P}_f corresponding to ocean hotspots but where the background characterization was successful but the potential fire pixel T_{MIR} was not high enough to pass the absolute threshold Tests 13a to 13d, a series of contextual threshold tests are used to test confirmation of the potential fire pixel.

In addition to the unaltered Test 14a, slightly lowered thresholds are used with the ocean equivalents for Tests 14b to 14f (termed for the ocean Tests 14b' to 14f'). This is possible due to the oceanic background being considerably more uniform than the land surface, and is necessary due to the typically relatively small increases in the thermal signals representative of gas offshore flares. Additionally, two further tests are employed over the ocean (Tests 14g and 14h):

$$L_{RED/MIR} > \bar{L}_{RED/MIR} \quad (14a')$$

$$\Delta T_{MIR-TIR} > \Delta \bar{T}_{MIR-TIR} + 2\sigma_{\Delta T_{MIR-TIR}} \quad (14b')$$

$$\Delta T_{MIR-TIR} > \Delta \bar{T}_{MIR-TIR} + 2.5K \quad (14c')$$

$$T_{MIR} > \bar{T}_{MIR} + 2\sigma_{T_{MIR}} \quad (14d')$$

$$T_{TIR} > \bar{T}_{TIR} - 2K \quad (14e')$$

$$\sigma'_{MIR} > 3.5K \quad (14f')$$

$$L_{SWIR1} > \bar{L}_{SWIR1} + 2 \times \sigma L_{SWIR1} \quad (14g)$$

$$L_{SWIR2} > \bar{L}_{SWIR2} + 2 \times \sigma L_{SWIR2} \quad (14h)$$

A daytime potential oceanic fire pixel from the set \mathcal{P}_f will be classified as a confirmed fire pixel if:

{The absolute threshold Test (13a) is true}

or

{Tests (14a') – (14d') are true; and Tests (14g) – (14h) are true; and either [Test (14e) or Test (14f) is true]},

otherwise it is classified as a non-fire pixel.

A nighttime potential fire pixel is classified as a true fire pixel if:

{The absolute threshold Test 13b is true or Tests 13c and 13d are true}

otherwise it is classified as a non-fire pixel

At potential oceanic fire pixels from the set \mathcal{P}_f where the background characterization failed, i.e. due to an insufficient number of valid background pixels being identified in the background window, only Tests (13a to 13c) can be applied. In this case if any of the relevant Tests (13a to 13d) are true then the pixel is classified as a fire pixel, otherwise the pixel is classified as “unknown”.

Furthermore, though it seems likely that nighttime fires will be more detectable in S6 than S5, it might be that some noise characteristics of the S6 channel make the additional use of the S5 band attractive. Test 13c could also therefore be repeated with data from the S5 band, both over ocean and over land.

7 ASSUMPTIONS AND LIMITATIONS

Main Assumptions

- Unsaturated, spatially co-located data from all channels required by the algorithm are available.
- Pixels containing cloud and water bodies have been masked out before the algorithms application, though pixels containing smoke remain unmasked.
- The SLSTR radiance measurements are well calibrated across the full range of spectral radiances measured over active fire pixels and background pixels.
- Duplicate pixels created during the data remapping process at level 1 will be identified as such so that duplicate fire pixels can be removed if desired.
- The area of the Earth (in m²) covered by each SLSTR pixel to be processed is available to the algorithm.
- An estimate of the atmospheric transmissivity in the SLSTR MIR channel is available to the algorithm, together with an estimate of the uncertainty in this value.
- The algorithm ignores the effects of increased aerosol and trace gas concentration above fires on the atmospheric transmissivity in the MIR channel (and indeed other channels).
- The fire and background emission are isotropic and approximate greybodies.
- The Planck's radiation law is well approximated by a fourth order power law in the wavelengths that the MIR channel of SLSTR is sensitive to.
- The pixel fire fraction can be neglected in the calculation of FRP.
- The fire pixel background radiance can be estimated from the radiance of the surrounding non-fire pixels.

Main Limitations

- The smallest/most weakly burning component of the fire regime will not be able to be detected with the moderate spatial resolution SLSTR instrument (fires covering down to perhaps 10⁻³ - 10⁻⁴ of a pixel will however be detectable). Access to the original

non-averaged data from the F1 and F2 detectors would improve the detectability of small fires significantly.

- The FRP for a fire pixel may have some dependence on where the sub-pixel sized fire lies within the pixel area.
- The overpass time of the Sentinel-3 satellite is non-optimum for capturing the peak of the fire diurnal cycle (Figure 2).

8 INPUTS AND OUTPUTS

Inputs (at each SLSTR pixel)

- Cloud masked radiances and reflectances in the SLSTR Optical Channels
- Radiances and brightness temperatures in the SLSTR Thermal Channels
- Pixel coordinates (latitude/longitude)
- Water vapor fields
- Satellite zenith angles
- Solar zenith angles
- Ground pixel (km^2)
- Mask representing the land area potentially capable of supporting land based hotspots (i.e. the land surface with larger lakes and rivers masked out).
- Mask representing the location of industrial hotspots and volcanically active zones
- Mask representing the area of oceans and large lakes that might potentially be the sites of offshore gas flares.

Suggested Outputs

At each detected fire pixel

- Hotspot pixel coordinates (column/row and latitude/longitude)
- Hotspot date and time
- FRP (MW)
- FRP uncertainty (MW)
- Fire pixel confidence
- Hotspot class (land hotspot in industrial region, land hotspot in volcanic region, vegetation fire, oceanic hotspot, unknown)
- Atmospheric transmittance
- Ground pixel area (km^2)
- Size of background window (b_w)
- Satellite zenith angle
- MIR brightness temperature of fire pixel
- TIR brightness temperature of fire pixel
- Mean MIR brightness temperature of the valid background window pixels
- Mean TIR brightness temperature of the valid background window pixels

Raster mask covering the entire SLSTR scene classified into the following classes: cloudy land pixels; cloud free land pixels; cloudy water pixels; cloud free water pixels; confirmed fire pixels coded according to the hotspot class (land hotspot in industrial region, land hotspot in volcanic region, vegetation fire, oceanic hotspot, unknown). This raster mask would compress to a small size and could be similar to that used in the MOD14 and MYD14 MODIS Fire Products (Giglio et al., 2003).

9 VALIDATION

The Level 1 datasets used for SLSTR processor evaluation are totally artificial and therefore of relatively little use in terms of validation. Here we instead include an example of the algorithm applied to MODIS imagery, which has somewhat similar spatial resolution, spectral bands and swath width to the SLSTR nadir view. As is apparent - large numbers of fire pixels are identified in this MODIS subscene.

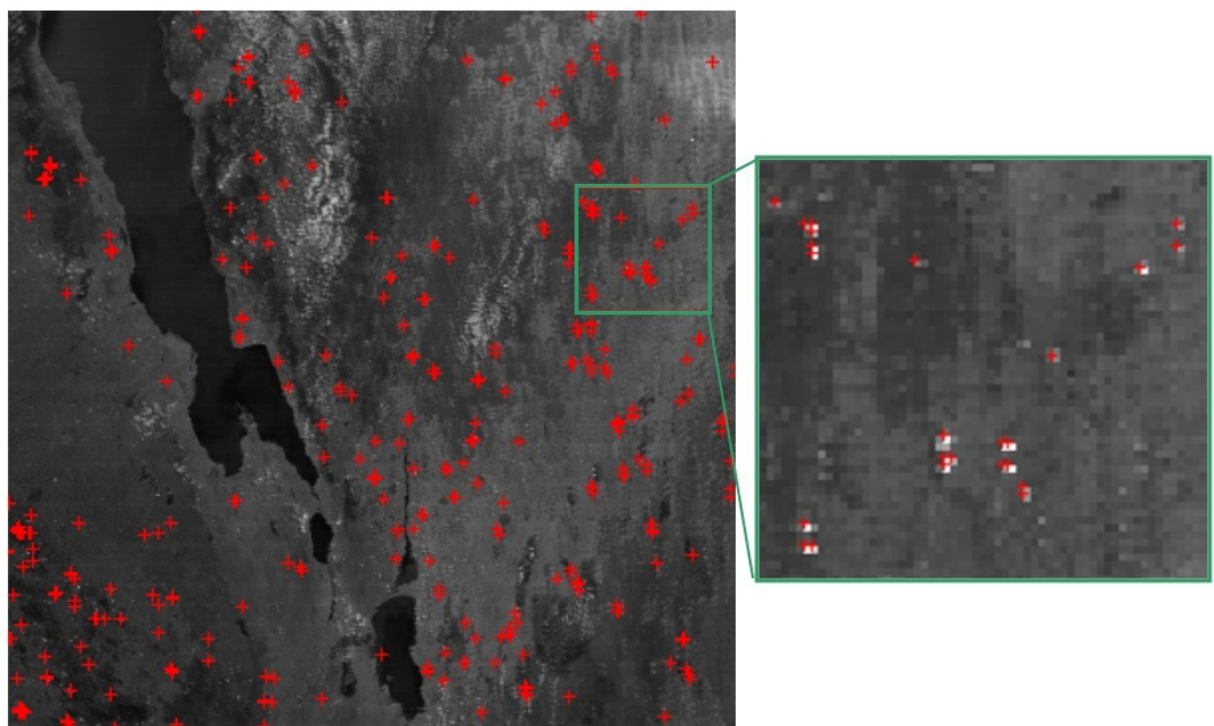


Figure 8: Example of fire detection result by day near Lake Malawi, Africa. Data is from EOS Aqua MODIS. Red crossed indicates detection location. Background image is the MIR – TIR brightness temperature difference image

In terms of the potential algorithm evolution to capture oceanic hotspots, the following figures include validation of that concept and the necessary algorithm adjustments, again applied to MODIS imagery.

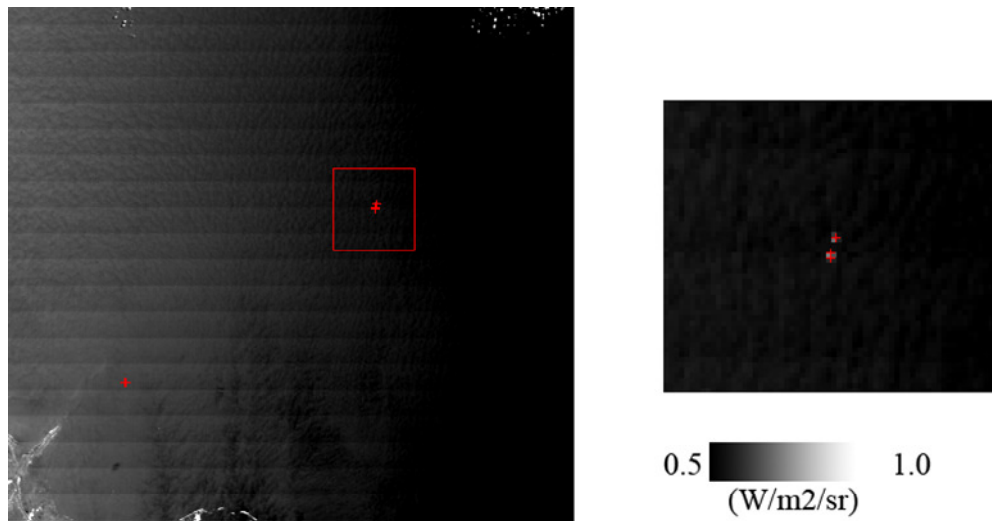
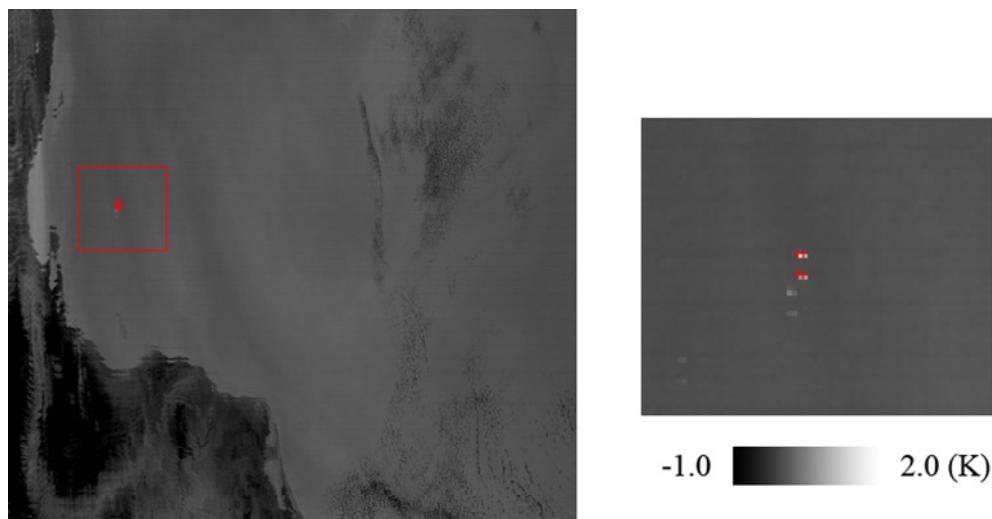


Figure 9: Gas flares detected by day in the Gulf of Mexico. Data is from EOS Aqua MODIS (18:55 UTC; 2 April 2005). Red crossed indicates detection location. Background image is the MIR – TIR brightness temperature difference image.



Gas Flare detected near Negeria (00:30 1 Aug 2008 UTC on Aqua)

Figure 10: Gas flares detected by night off Nigeria. Data is from EOS Aqua MODIS (00:30 UTC; 1 August 2008). Red crossed indicates detection location. Background image is the MIR – TIR brightness temperature difference image.

10 REFERENCES

Arino, O., S. Plummer and S. Casadio (2007). Fire Disturbance: the Twelve years time series of the ATSR World Fire Atlas. Proceedings of the ENVISAT Symposium 2007, SP-636, ESA

Bond W.J. and van wilgen B.W. (1996). Fire and Plants. London: Chapman and Hall.

Csiszar, I. Arino, O., Geraci, R., Giglio, L., Goldammer, J., Justice, C., Kondragunta, S., Prins, E., Sessa, R., Tansey, K., and Wooster, M. (2008). Essential Climate Variable: Fire Disturbance, GTOS Report ECV T13 (<http://www.fao.org/GTOS/ECV-T13.html>)

Csiszar, I., Denis, L., Giglio, L., Justice, C.O., Hewson, J. (2005). Global fire activity from two years of MODIS data. International Journal of Wildland Fire, 14:117-130.

Dennison, P.E., K. Charoensiri, D.A. Roberts, S.H. Peterson, and R.O. Green (2006). Wildfire temperature and land cover modeling using hyperspectral data. Remote Sensing of Environment, 100, 212-222

Dozier, J. (1981). A method for satellite identification of surface temperature fields of subpixel resolution. Remote Sensing of Environment, 11:221-229.

Flasse, S. P. and P. Ceccato a (1996). A contextual algorithm for AVHRR fire detection. International Journal of Remote Sensing, Volume 17, Issue 2 January 1996 , pages 419 - 424

Freeborn, P.H., Wooster, M.J., Hao, W.M., Ryan, C.A., Nordgren, B.L. Baker, S.P. and Ichoku, C.(2008). Relationships between energy release, fuel mass loss, and trace gas and aerosol emissions during laboratory biomass fires, J. Geophys. Res., Vol. 113, No. D1, D01102, 10.1029/2007JD008489.

Fuller Douglas O. (2000). Satellite remote sensing of biomass burning with optical and thermal sensors, Progress in physical geography, vol. 24, no4, pp. 543-561.

Gallegos, S., Ryan, R., Holekamp, K., Baud, R. and Bloemker, J. (2007) MODIS products to improve the monitoring of gas flaring from offshore oils and gas facilities, Final Repor to NASA Science Mission Directorate, 10pp.

Generoso, S., Bréon, F.M, Balkanski, Y., Boucher, O. and Schulz, M.(2003). Improving the seasonal cycle and interannual variations of biomass burning aerosol sources, *Atmos. Chem. Phys.* 3, 1211-1222.

Giglio, L. (2005). MODIS Collection 4 Active Fire Product User's Guide Version 2.2, NASA [Online] Available: <http://modis-fire.umd.edu/products.asp>

Giglio, L. and J. D. Kendall (2001). Application of the Dozier retrieval to wildfire characterization—A sensitivity analysis. *Remote Sens. Environ.*, vol. 77, 1226 no. 1, pp. 34–49.

Giglio, L. and Justice, C. (2003). Effect of wavelength selection on characterization of fire size and temperature, *IJRS*, 24, 3515-3520

Giglio, L. and Kendall, J. D. (2001). Application of the Dozier retrieval to wildfire characterization: A sensitivity analysis. *Remote Sensing of Environment*, 77:34-49.

Giglio, L. J. D. Kendall, and C. O. Justice (1999). Evaluation of global fire detection algorithms using simulated AVHRR infrared data. *Int. J. Remote Sens.*, vol. 20, no. 10, pp. 1947–1985.

Giglio, L. J. D. Kendall, and R. Mack (2003a). A multi-year active fire dataset for the tropics derived from the TRMM VIRS. *Int. J. Remote Sens.*, vol. 24, no. 22, pp. 4505–4525.

Giglio, L., Csiszar, I., Justice, C.O. (2006a). Global distribution and seasonality of active fires as observed with the Terra and Aqua MODIS sensors. *Journal of Geophysical Research - Biogeosciences*, Vol 111, doi:10.1029/2005JG000142

Giglio, L., J. Descloitres, C. O. Justice, and Y. J. Kaufman (2003b). An enhanced contextual fire detection algorithm for MODIS. *Remote Sens. Environ.*, vol. 87, no. 2/3, pp. 273–282.

Giglio, L., van der Werf, G. R., Randerson, J. T., Collatz, G. J., and Kasibhatla, P. S. (2006b). Global estimation of burned area using MODIS active fire observations. *Atmospheric Chemistry and Physics*, 6:957-974.

Ichoku, C. and Y.J.Kaufman, L. Giglio, Z. Li, R.H. Fraser, J.Z.Jin, and W.M.Park, (2003). Comparative analysis of daytime fire detection algorithms using AVHRR data for the 1995 fire season in Canada: perspective for MODIS. *Int.J. Remote Sensing*, vol.24, no.8 pp. 1669-1690.

Ichoku, C., Kaufman, Y.J. (2005). A method to derive smoke emission rates from MODIS fire radiative energy measurements. *Geoscience and Remote Sensing, IEEE Transactions on* Volume 43, Issue 11, 2636 – 2649 DOI:10.1109/TGRS.2005.85732

Jordana, N.S., Charles Ichokub, C and Raymond M. Hoffa (2007). Estimating smoke emissions over the US Southern Great Plains using MODIS fire radiative power and aerosol observations. *Atmospheric environment*, Volume 42, Issue 9, March 2008, Pages 2007-2022

Justice, C. O., Giglio, L., Korontzi, S., Owens, J., Morisette, J. T., Roy, D., et al. (2002). The MODIS fire products. *Remote Sensing of Environment*, 83, 244–262.

Kaufman, Y.J. R.G. Kleidman and M.D. King (1998). SCAR-B fires in the tropics: properties and remote sensing from EOS-MODIS, *Journal of Geophysical Research* 103, pp. 31955–31968.

Kaufman, Y.J., Justice, C.O., Flynn, L.P., Kendall, J.D., Prins, E.M., Giglio, L., Ward, D.E., Menzel, W.P., and Setzer, A.W. (1998). Potential global fire monitoring from EOS-MODIS. *Journal of Geophysical Research*, 103:32,215-32,238.

Lavorel, S., Flannigan, M., Eric F. Lambin, Mary C. Scholes (2006). Vulnerability of land systems to fire: Interactions among humans, climate, the atmosphere, and ecosystems. *Mitig Adapt Strat Glob Change*, DOI 10.1007/s11027-006-9046-5

Levine, J. (1996). *Biomass Burning and Global Change: Remote sensing, modeling and inventory development, and biomass burning in Africa*, MIT Press, 1996, 551pp

Loboda, T. and Csiszar, I. (2007). Reconstruction of Fire Spread within Wildland Fire Events in Northern Eurasia from the MODIS Active Fire Product. *Global and Planetary Change*, 56 (3-4): 258-273 .

Roberts, G. and Wooster M.J. (2008). Fire detection and fire characterization over Africa using Meteosat SEVIRI. *IEEE Transactions on Geoscience and Remote Sensing*, 46, 1200-1218, doi: 10.1109/TGRS.2008.915751

Roberts, G., Wooster, M.J., Perry, G.L.W., Drake, N., Rebelo, L-M., Dipotso, F. (2005). Retrieval of biomass combustion rates and totals from fire radiative power observations: Application to southern Africa using geostationary SEVIRI Imagery. *Journal of Geophysical Research*, 110, D21111, doi: 10.1029/2005JD006018

Robinson, J.M. (1991). Fire from the space: Global fire evaluation using infrared remote sensing. *Int. J. Remote sensing*, vol.12, no.1 pp. 3-24.

Schaaf, C. (2008). Albedo and Reflectance Anisotropy, Terrestrial Essential Climate Variables for Climate Change Assessment, Mitigation and Adaptation. GTOS-52, Eds. R. Sessa and H. Dolman, FAO, Rome, 28-29.

Schultz, M. (2002). On the use of ATSR fire count data to estimate the seasonal and interannual variability of vegetation fire emissions. *Atmos. Chem.Phys.*, vol. 2, no. 5, pp. 387–395.

Sinha, P., Jaeglé, L., Hobbs, P.V. and Q. Liang (2004). Transport of biomass burning emissions from southern Africa, . *J. Geophys. Res.*, 109, D20204, doi:10.1029/2004JD005044.

Sukhinin, A. I. Nancy H.F. French,, Eric S. Kasischke, Jenny H. Hewson, Amber J. Soja, Ivan A. Csiszar, Edward J. Hyer, Tatiana Loboda, Susan G. Conrad, Victor I. Romasko, Eugene A. Pavlichenko, Sergey I. Miskiv and Olga A. Slinkina (2004). AVHRR-based mapping of fires in Russia: New products for fire management and carbon cycle studies, Volume 93, Issue 4, Pages 546-564

Sullivan, A. L., P. F. Ellis and I. K. Knight (2003). A review of radiant heat flux models used in bushfire applications, *international Journal of Wildland Fire*. 12(1) 101 – 110

Thompson, A.M., Witte, J.C, Hudson, R.D., Guo, H., Herman, J.R., Fujiwara, M. (2001). Tropical Tropospheric Ozone and Biomass Burning. *Science*, 291, 16.

Van der Werf, G.R., J.T. Randerson, L. Giglio, G.J. Collatz, P.S. Kasibhatla (2006). Interannual variability in global biomass burning emissions from 1997 to 2004. *Atmos. Chem. Phys. Discuss.*, 6, 3175-3226.

Wooster, M.J. and Strub, N. (2002). Study of the 1997 Borneo Fires: Quantitative analysis using Global Area Coverage GAC. satellite data, *Global Biogeochemical Cycles* 161: doi:10.1029/2000GB001357

Wooster, M.J., B. Zhukov, and D. Oertel (2003). Fire radiative energy for quantitative study of biomass burning: Derivation from the BIRD experimental satellite and comparison to MODIS fire products, *Remote Sens. Environ.*, 1410 vol. 86, no. 1, pp. 83–107.

Wooster, M.J., G. Roberts, G. L. W. Perry, and Y. J. Kaufman (2005). Retrieval of biomass combustion rates and totals from fire radiative power obser vations: FRP derivation and calibration relationships between biomass consumption and fire radiative energy release. *J. Geophys. Res.*, vol. 110, no. D24, p. D24 311, DOI:10.1029/2005JD006318.

Wooster, M.J., Zhukov, B. and Oertel, D. (2003). Fire radiative energy for quantitative study of biomass burning: Derivation from the BIRD experimental satellite and comparison to MODIS fire products. *Remote Sensing of Environment* 86: 83-107.

Xie, Y., Qu, J.J., Hao, W., Che, N., and Sommers, E. (2007). Smoke plume detection in the eastern United States using MODIS. *International Journal of Remote Sensing*, Volume 28 , Issue 10, Pages 2367-2374

Zhukov, B., Lorenz, E., Oertel, D., WOOSTER, M.J. and Roberts, G. (2006). Space borne detection and characterization of fires during the Bi-spectral Infrared Detection (BIRD) experimental small satellite mission 2001-2004. *Remote Sensing of Environment* 100: 29-51.

11 APPENDIX A: SENTINEL-3 SLSTR CHANNEL NAMING CONVENTION

SLSTR Channel Name	Used for Spectral Radiance (L) and/or Brightness Temperature (T) and or Spectral Reflectance (ρ) Measure in ATBD	Central Wavelength (μm)	Waveband Width (μm)	Spatial Sampling Distance (Nadir Swath / km)
S1	-	0.555	0.02	0.5
S2	L_{RED} and ρ_{RED}	0.659	0.02	0.5
S3	ρ_{NIR}	0.865	0.02	0.5
S4	-	1.375	0.015	0.5
S5	L_{SWIR1}	1.61	0.06	0.5
S6	L_{SWIR2} and ρ_{SWIR2}	2.25	0.05	0.5
S7	L_{TIR} and T_{TIR}	3.74	0.38	1.0
S8	L_{TIR} and T_{TIR}	10.95	0.9	1.0
S9	T_{TIR2}	12	1.0	1.0
F1	L_{MIR} and T_{MIR}	3.74	0.38	1.0
F2	L_{TIR} and T_{TIR}	10.95	0.9	1.0

Note that the F1 and F2 ‘fire channels’ have greatly increased saturation temperatures compared to the matching standard (‘S’) IR channels operating at the same wavelengths (S7 and S8), though at the expense of increased noise characteristics. This is to allow unsaturated observations to be made at even very strongly radiating fire pixels. It is therefore expected that L_{MIR} and T_{MIR} will be derived from the S7 and S8 channels where unsaturated observations are available, with observations from F1 and F2 being used only at pixels where saturation occurs. Due to the spectral emission characteristics of vegetation fire (Figure 3) saturation is expected to occur much more frequently at MIR wavelengths than at TIR wavelengths, so much more use is expected of the F1 channel than the F2 channel.